Insight into the fracture behaviour and mechanical response of ECAP processed cast and LPBF AlSi10Mg alloy

Krzysztof Żaba, Przemyslaw Snopiński, Daniel Walach, Grzegorz Piotr Kaczmarczyk, Stanislav Rusz

Insight into the fracture behaviour and mechanical response of ECAP processed cast and LPBF AlSi10Mg alloy

Krzysztof Żaba[1], Przemysław Snopiński[2,*], Daniel Wałach[3], Grzegorz Piotr Kaczmarczyk[3], Stanislav Rusz[4]

[1] Department of Metal Working and Physical Metallurgy of Non-Ferrous Metals, AGH University of Science and Technology, Al. Adama Mickiewcza 30, 30-059 Cracow, Poland

[2] Department of Engineering Materials and Biomaterials, Silesian University of Technology, Akademicka 2A, 44-100 Gliwice, Poland

[3] Department of Geomechanics, Civil Engineering and Geotechnics, AGH University of Science and Technology, Al. Mickiewicza 30, 30-059 Cracow, Poland

[4] Department of Mechanical Technology, VŠB—Technical University of Ostrava, 17 Listopadu 15, 708-33 Ostrava-Poruba, Czech Republic

Corresponding author e-mail: przemyslaw.snopinski@polsl.pl

Abstract

This paper presents a comparative analysis of the microstructure, tensile deformation and fracture mechanisms of an ECAP-processed AlSi10Mg alloy produced by two different methods: selective laser melting (SLM) and casting. The evolution of the microstructure was investigated using optical microscopy (OM), scanning electron microscopy (SEM) and electron backscatter diffraction (EBSD). In addition, internal structural defects were analysed using X-ray computed tomography scans (CT). To investigate the mechanical properties and crack propagation during tensile deformation, a real-time visualization through in-situ tensile CT scans, along with the loading-unloading-reloading tensile test (LUR) was employed. The results showed significant differences in the mechanical property between the two ECAP-processed samples. Specifically, the SLM sample exhibited an approximately 50% higher tensile strength of 370 MPa and a remarkable elongation at break of 12%. Detailed microstructural analysis showed that the additional work hardening occurred mainly in the hetero-zones, where the accumulation of geometrically necessary dislocations developed back and forward stresses, which together led to the hetero-deformation induced (HDI) stresses. Further quantification of the (HDI) stress derived from the loading-unloading-reloading tensile test (LUR) confirmed origin of the additional strain hardening in the SLM specimen. Fractographic analysis showed that the poor tensile ductility of the ECAP-processed cast specimen was primarily due to the low bonding between Al and Si particles, resulting in premature fracture. In contrast, the ECAP-processed SLM specimen fractured predominantly along the softer heat-affected zones (HAZ).

Keywords: AlSi10Mg alloy, Selective Laser Melting, Casting, Computed tomography, Fracture mechanisms, HDI stress

1. Introduction

Aluminium alloys are becoming increasingly popular in the automotive, transportation, aerospace, and railroad industries [1] [2]. This is due to their remarkable ability to significantly reduce weight, leading to improved fuel efficiency and subsequent reduction in CO_2 emissions [3]. Among the various aluminium alloys available, those enriched with silicon, such as AlSi7Mg, AlSi10Mg and Al-12Si, are of particular interest [4]. These alloys have a considerable volume fraction of eutectic Al-Si, which contributes to their favourable weight-to-resistance ratio; therefore, are well suited for the manufacture of a variety of components, including supports, housings, brackets, panels, and actuators [5].

Al-Si alloys were originally developed for casting processes that offer advantages in terms of cost efficiency and mass production. However, the advent of additive manufacturing (AM) has introduced a new paradigm in alloy production that offers distinct advantages and opportunities for Al-Si alloys. It enables the improvement of mechanical properties as well as the development of lighter structures through topological optimization or lattice structures [6].

The layer-by-layer thermal cycle, the targeted energy input, and the rapid cooling of AM affect the microstructure and properties of AM alloys, making them distinct from their cast counterparts. According to the literature, the microstructures of cast alloys are composed of α-Al dendrites and eutectic silicon, which has a thin flake morphology with a high aspect ratio and a needle-like shape. This specific morphology of eutectic silicon can cause stress concentrations that negatively affect the mechanical properties of the alloy (making it brittle) [7,8]. Fracture and detachment of silicon particles are the main factors that influence the fracture resistance of Al-Si castings [9,10]. Therefore, the Al-Si alloys are usually heat treated [11] or inoculated [12,13] to modify the Si morphology.

The additively manufactured Al-Si alloys have a much finer grain size and a higher degree of silicon supersaturation than their cast counterparts [14]. In addition, the high cooling rate and nonequilibrium solidification during the LPBF process lead to a hierarchical and heterogeneous microstructures, which can be divided into the three leves. The first one is represented by the bimodal grain distribution. Columnar grains are predominant in the melt pool, while fine equiaxed grains exist along the boundaries of the melt pool (MPBs) [15]. The second one is represented by the mesoscale melt pool structure (MP), which can be divided into three zones: (i) melt pool coarse (MP coarse), (ii) melt pool fine (MP fine) and (iii) heat

affected zone (HAZ) [16,17]. The third one is represented by the ultrafine cellular network composed of Al and eutectic Si phases [18]. This distinctive hierarchical and heterogeneous structure affects the mechanical strength and fracture behaviour of LPBF-Al-Si alloys, as shown by the different tensile strength and elongation values of as-cast and LPBF specimens [19].

Similar to cast alloys, the additively manufactured Al-Si alloys undergo post-processing, which significantly affects their microstructure and mechanical properties. In the context of fracture behaviour, scientists have investigated the effects of various factors such as build directions [20], scanning strategy [21], heat treatments [22], thermomechanical processing [23] and surface severe plastic deformation [24]. Recent studies have also shown the effectiveness of bulk severe plastic deformation processes in improving the mechanical performance of additively manufactured Al-Si alloys. For example, Yusuf et al. [25] utilized high pressure torsion to post-process AM AlSi10Mg alloy, which resulted in a remarkable increase in hardness (from 140 to 220 HV) and improved microstructural homogeneity. Similarly, Hosseinzadeh et al. [26] used equal channel angular pressing (ECAP) for post-processing of AM AlSi12 alloy. They observed significant enhancements in yield strength (YS), ultimate tensile strength (UTS) and ductility, which increased by 56%, 11% and 55% to 420 MPa, 514 MPa and 5.5%, respectively, after four ECAP passes. Additionally, Snopinski et al. [27] performed post-processing ECAP on an AM AlSi10Mg alloy and reported a superior combination of strength and ductility after a single ECAP pass at 200 ºC.

Al As reported in the above mentioned studies, the SLM specimens that have undergone ECAP show a remarkable balance of strength and ductility, the cast counterparts have much lower levels of both strength and ductility [28–30]. Therefore, it is essential to understand how these different initial states affect the fracture mechanisms for optimizing the mechanical properties of materials processed by SPD techniques. This study aims to reveal the complex relationship between initial material states and fracture behaviour by conducting a rigorous analysis, exploring microstructural features, and investigating the mechanical response to external forces.

The primary objective of this study is to explore the impact of two initial material conditions (cast and SLM) and subsequent ECAP processing on the microstructure, deformation behaviour, and fracture mechanism. The paper is divided into four sections. The first section provides an introduction to the microstructural evolution of the cast and SLM specimens subjected to one ECAP pass at 300 ºC. In the second section, we present the reconstruction of

specimen surface and internal defects of the ECAP-processed specimens using optical 3D scanning and µCT images. The third section focuses on the evaluation of mechanical properties through in-situ µCT tensile tests. Lastly, the fourth section delves into the analysis of fracture mechanisms.

The findings of this research provide valuable insights into the fracture mechanics of ECAP-processed materials, elucidating the reasons behind the exceptional strength and ductility combination seen in SLM ECAP-processed samples and the relatively lower mechanical properties exhibited by their cast ECAP-processed counterparts.

The results of this study open up new possibilities for applying ECAP-processed additively manufactured AlSi10Mg alloy in various industries that require components that are lightweight, strong and corrosion-resistant. Moreover, the results can also stimulate further research on the combination of additive manufacturing and severe plastic deformation techniques such as ECAP to create novel components that need to withstand high loads and harsh environments. Furthermore, the results can also help to develop new design guidelines and optimization strategies for additive manufacturing and post-processing of AlSi10Mg and other similar alloys. Ultimately, these experimental results can provide valuable insights into the relationship between the processing parameters, microstructural features and mechanical behaviour of this alloy.

2. Methodology

2.1. Specimen fabrication

In this work the AlSi10Mg alloy specimens were fabricated by selective laser melting (SLM) and casting. In the case of SLM specimens, gas-atomized AlSi10Mg powder (depicted in Figure 1) was utilized, featuring a particle size distribution ranging from 20 to 90 µm. The specimens were 3D printed using the EOS M290 device, orienting them at a 90° angle with respect to the horizontal powder bed. The SLM process parameters are given in Table 1.

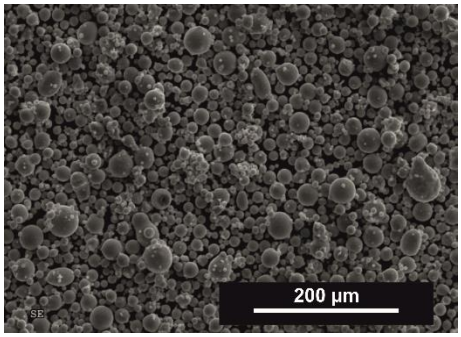

Fig. 1. SEM image of AlSi10Mg powder used in a current study.

Table 1. SLM process parameters

Scan speed [mm/s]	1300
Laser power [W]	310
Layer thickness [µm]	30
Protective atmosphere	Argon
Platform temperature [ºC]	200

To prepare the cast specimens, a mixture of pure aluminium (EN AW-Al99.98), technical pure silicon, and magnesium (EN-MB99.95-A) was utilized. The aluminium and silicon were placed directly in the crucible prior to the smelting process, while the magnesium was added to the liquid solution towards the end of the smelting process using a vacuum feeder. Smelting and casting were conducted at approximately 720 ºC. Subsequently, the molten alloy was carefully poured into pre-prepared moulds to achieve the desired specimen shapes. Figure 2 shows the specimens fabricated via casting and AM routes.

a) b)

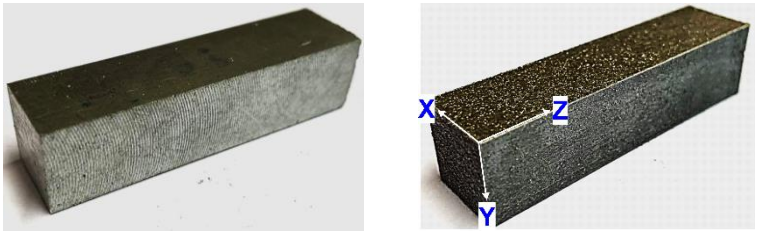

Fig. 2. Schematic illustration of the test specimens a) cast (after machining), b) SLM (as printed).

The ECAP experiment was performed using the LabTest 5.2000CT hydraulic press (depicted in Figure 3) controlled by Test Emotion software, which allowed the measurement of force values as a function of deformation resistance (σ) versus displacement (Δh).

Fig. 3. View of the workplace for material forming using the ECAP method.

The heating was controlled with a dTRON 304 device equipped using a NiCr-Ni thermocouple that can be used up to a maximum temperature of 1350 ºC. To minimize the friction between the ECAP specimen and the ECAP die a Nicro-Thermocup 1200 lubricant was applied. The specimens (14.25 × 14.25 × 60 mm) were then pressed once through a 90º die (introducing an equivalent strain of ε = ~1) at 300 ºC. Figure 4 shows the stress-displacement curves recorded during the ECAP processing.

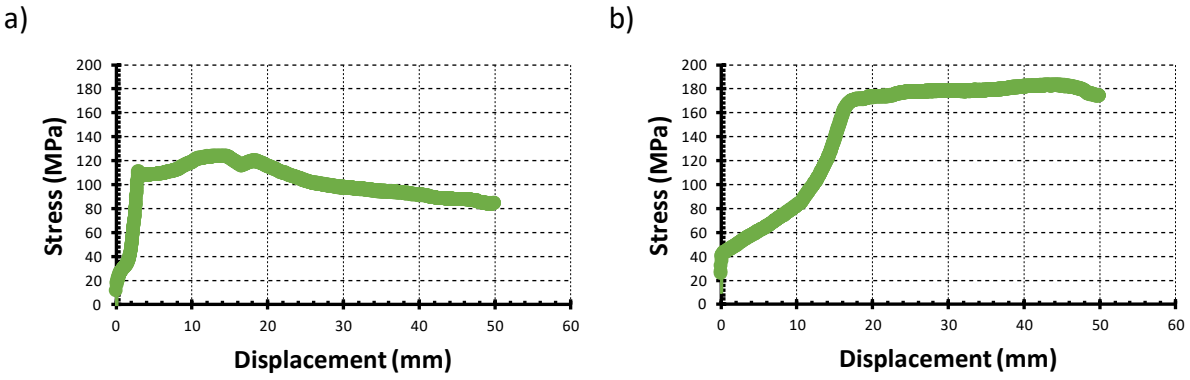

Fig. 4. Deformation resistance – displacement curves of a) ECAP-processed cast specimen, b) ECAP-processed SLM specimen.

The stress-displacement curves show that the ECAP process causes significant strain hardening. The load increases steadily as the displacement increases until the specimen is completely extruded through the corner of the ECAP die. Then, the load stays relatively stable. We notice that the cast specimen needs much less stress than the SLM specimen, which means that the SLM specimen deforms more. Moreover, the stress-displacement curve suggests that the cast specimen may undergo dynamic recovery (DRV) or dynamic recrystallization (DRX).

2.2. Microstructure characterization

Metallographic studies were conducted using a Zeiss Axio Observer Z1 light microscope. For light microscopy investigations, the specimens were prepared following standard metallographic procedures. This included grinding (with #500 and #1200 grit SiC papers) and polishing (with 6, 3 and 1 µm diamond pastes) the specimens to achieve a suitable mirror-like surface finish. The metallographic specimens were etched with Keller's reagent (2.5 ml HNO_3 1.5 ml HCl 1 ml HF 95 ml) for 60 seconds.

For EBSD analyses, a ZEISS Supra 35 microscope was employed with specific operating parameters, including an accelerating voltage of 15 kV, a working distance of 17 mm, a tilt angle of 72º, and a step size of 0.12 µm. Specimen preparation for SEM followed the same procedure as for LM, with additional fine polishing with 0.04 µm colloidal silica for 1 hour. This additional polishing step was performed to reduce surface roughness and thus improve the quality of the EBSD signal. The grain size was determined according to ASTM E112-96 standard.

2.3. µCT measurements

CT the examinations were performed using X-ray computed tomography technique. The tomographic analysis process is based on three main successive tasks: Acquisition of X-ray projections, reconstruction of 3D volumes, and volumetric analysis. In addition, in-situ tensile tests were conducted. After the initial tomographic analysis (gray-colored path in Figure 5), the specimens were trimmed to the dimensions suitable for the tensile tests (green coloured path). The tomographic analysis during the tensile test is performed in successive load levels:

1) The specimen is stretched until a predetermined force threshold is reached, whereupon the actuator is stopped.

2) Then the specimen is topographically scanned while rotating 360 degrees around the vertical axis.

3) After scanning, the stage is activated again.

4) Once the next force level is reached, another tomographic measurement is taken.

5) After tensile test, a final measurement is made with the area of interest focused on the fracture surface.

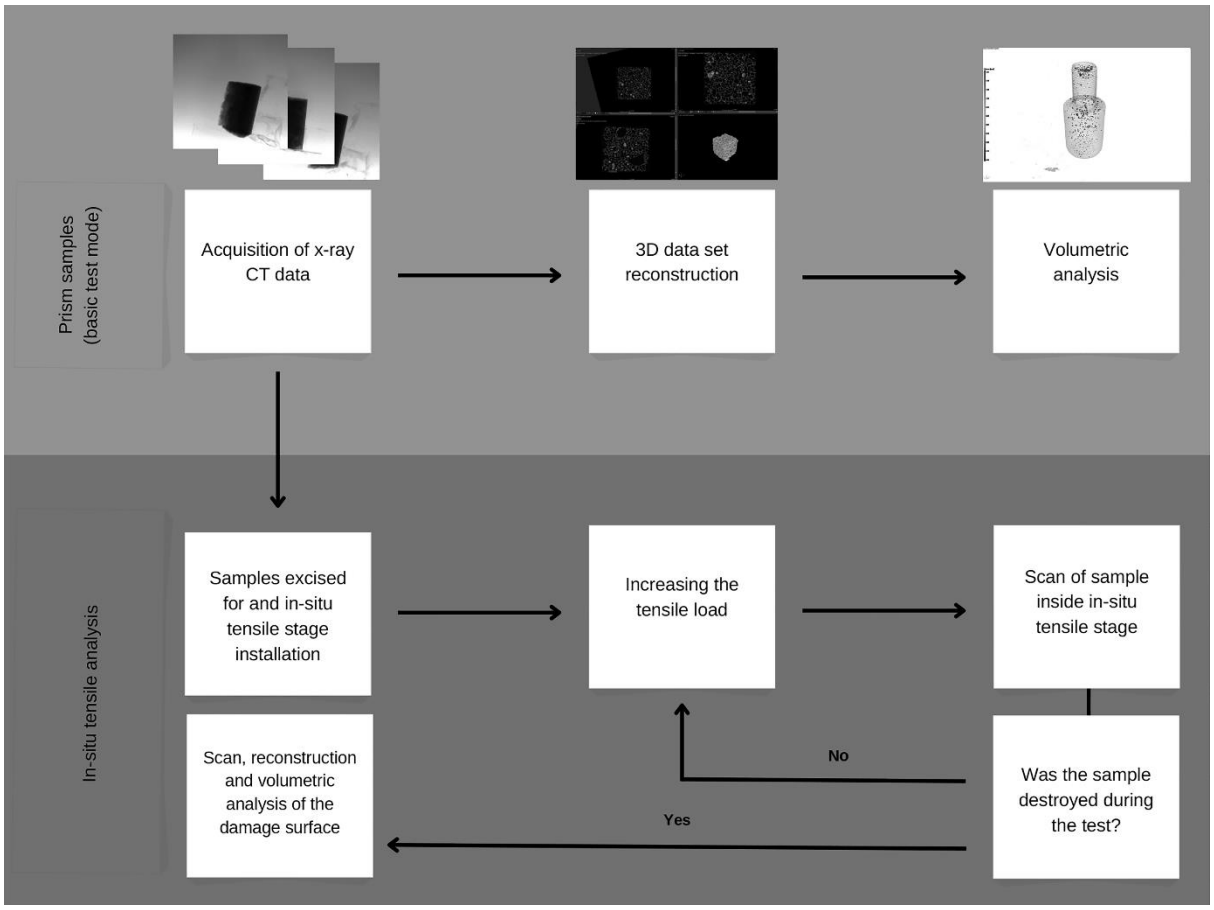

Fig. 5. Schematic illustration of µCt investigation.

The µCT measurements were made on a Phoenix v | tomex m300 device (Fig. 6) using a microfocus lamp. The tested material was characterized by a similar absorption of X-ray waves, which means that from the point of tomographic examination two groups of elements can be distinguished:

- Elements with a rectangular cross-section - tested according to the lamp parameters: 120 kV, 300 µA, magnification 4.00x, voxel size 50 µm,
- Square section elements - tested according to the lamp parameters: 210 kV, 150 µA, magnification 2.67x, voxel size 75 µm.

All specimens required the use of a 0.5 mm Sn filter. The detector in each position made 4 measurements - one was omitted and three averaged. The exposure time for one measurement was set to 333 ms. The signal amplification factor was set at 0.500 on the manufacturer's scale. In the reconstruction process, specimen shifts were optimized based on the initial measurements made by the device. A shift of 0.2 px was assumed as the limit value which allowed the study to be analyzed. Each time the virtual axis of rotation was corrected. The beam amplification corrections were applied according to the bhc + algorithm, degree 7.4.

The defect analysis was performed in the VG Studio MAX 3.4 software. The detection was performed according to the VGDefx / Only threshold formula. Image analysis parameters and filtering criteria were adjusted individually to the obtained data based on the absorption histograms.

Specimens were scanned utilizing consistent parameters, Table 2, yielding reconstructed datasets with uniform isosurface values for the material in question. This uniformity in scanning parameters affords the advantage of facilitating defect analysis under stable input conditions. Consequently, the volumes of defects ascertained can be directly compared across different specimens. During the study, porosity analysis was conducted using the built-in features of VG Studio 3.4. The VGDefX analysis operates on the principle of detecting signal level reductions within the examined data. A threshold value of approximately 55.000 was established as the maximal void indicator. All locations identified by the algorithm as potential defects are subjected to a filtering process. In terms of size, it was determined that the minimum volume for a defect should consist of 8 voxels. This filtering criterion is instrumental in eliminating noise and the erroneous detection of natural variations within the sample. Subsequently, a visual assessment of cross-sections is imperative to ascertain the inclusion of all defects. Should noise erroneously classified as part of the analysis results be discovered, manual exclusion of such defects from the solution set is possible. Porosity analysis in homogeneous materials is extensively applied in material analysis studies, as evidenced by the literature [31].

Fig. 6. Phoenix v|tomex m300 with DEBEN CT5000TEC control module.

Table 2. The main parameters used in µCT measurements

Parameter	**Cross-section of the sample**	**Samples with a rectangular cross-section**	**In-situ tests**	**Post in-situ scans**
Tube	Microfocus			
Voltage [kV]	210	120	120	60
Current [µA]	140	300	150	100
Exposure Time [ms]	333	250	84	150
Number of Projections	2500	2100	1400	3000
Signal Amplification Factor	0.50	0.50	0.50	1.00

2.4. Mechanical properties evaluation

Tensile strength tests were conducted in-situ within the tomographic chamber using the DEBEN CT-5000TEC stage. The strength parameters were investigated using two types of specimens. Specimens with a circular notch (Figure 7(a)) were employed to determine the tensile strength of the tested materials at a controlled point of failure, specifically, the minimum cross-sectional area. Conversely, specimens featuring the configuration depicted in Figure 7(b) were utilized for cyclic loading-unloading tests, aimed at elucidating the strain hardening mechanisms of materials subjected to ECAP processing. The cyclic loading tests were conducted with a constant strain increment until specimen failure occurred. For each prescribed strain value, scans were performed, corresponding to characteristic stress drop occurrences on the stress-strain curve.

The specimen was securely held in place using special jaws, which were centered with pins and then tightened with screws. The configuration of the specimen connection is depicted in Figure 7(c), where the upper part of the specimen is fully mounted, while the lower part is shown prior to tightening the second set of jaws. It is important to note that the entire stage is positioned within the tomography chamber, Fig. 7(d).

The use of vitreous glassy carbon in the construction of the stage is greatly appreciated, as it is a highly durable material with low X-ray absorption properties. This feature allows for the examination of the internal structure of the specimen. The initial position of the stage, "before the test," is illustrated in Figure 7(c), providing a visual reference for the experimental setup.

The specimens were tested with the following lamp parameters: 120 kV, 150 µA, magnification of 6.667 and a voxel size of 30 µm. During the tensile test, the upper jaws remain stationary while the lower jaws are displaced downward

a) b)

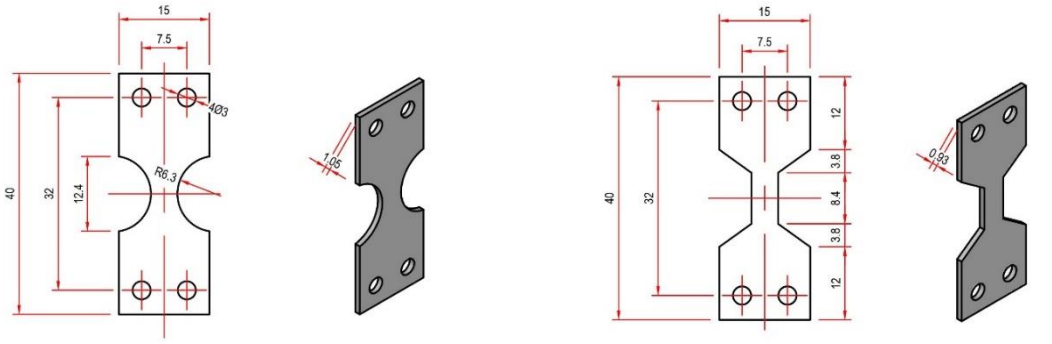

c) d)

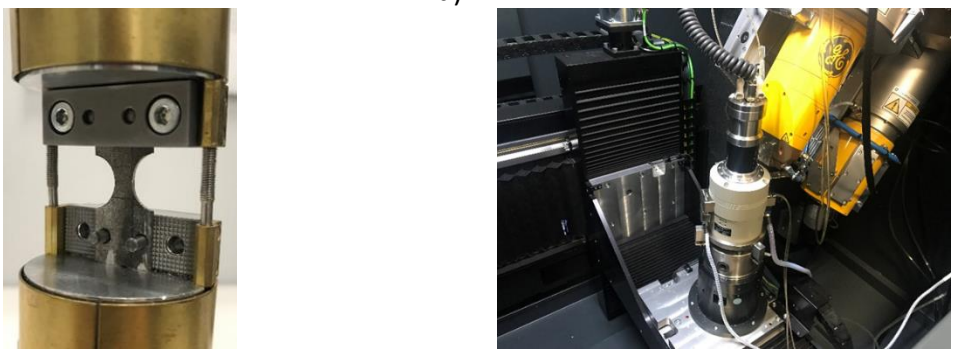

Fig. 7. µCT in-situ tensile test a) specimen geometric dimensions - specimens applied to determine the tensile strength (in mm), b) , specimen geometric dimensions - specimens used in cyclic studies, c) specimen mounting, d) position of the stage in the tomography chamber.

Throughout the entire study, in addition to X-ray projections, the displacement of jaws (specimen elongation) and the applied force were recorded. Tomographic measurements were conducted at individual points. An exemplary force - elongation graph is presented in Figure 14. The graph displays positions where a decrease in force was observed. These drops are associated with relaxation [32].

After the specimen fractured, it was removed from the device. One of the damaged fragments was then scanned at a high magnification of approximately 33.000, with a voxel dimension of 6 µm. The radiation used for the scan was generated by a microfocus lamp with characteristics of 60 V and 100 µA.

3. Results

3.1. Microstructure analysis

Figure 8 shows optical micrographs of the tested specimens. These images reveal diverse microstructures resulting from the different manufacturing processes (casting and SLM). As can be seen, the microstructure of the cast alloy (Fig. 8(a)) exhibits primary α-Al dendrites surrounding interconnected eutectic Si and Mg_2Si phases [33] [34]. In contrast, the SLM alloy (Fig. 8(b)) exhibits overlapping laser scan paths with a width of 100-120 µm. This unique pattern results from the successive 90º rotation in the scan direction for each layer.

The optical microstructure of the cast AlSi10Mg alloy in the X–Y plane (i.e., the flow plane) after ECAP processing is shown in Fig. 8(a). As can be seen, the shear stress produced by the first ECAP pass alters the dendritic structure of the cast specimen. As a result, thin, elongated, parallel shear bands with a specific direction were generated (see yellow arrows). Moreover, the primary α-Al dendrites have become elongated and “pancaked”. Also noteworthy are the significant changes in the morphology and size of the eutectic Si particles, which exhibit enhanced fragmentation after the ECAP process. Supplementary Figures S1(a) and (b) show a more detailed representation of the effects of ECAP on the morphology of particles in the eutectic region.

The microstructural evolution of the SLM AlSi10Mg alloy differs significantly from that of the cast counterpart and exhibits unique features. After a single ECAP pass, semi-circular "fish scale" patterns (indicated by dashed lines in Fig. 8(d)) replace the overlapping laser scan paths visible in the microstructure of the unprocessed specimen. The effect of the ECAP processing on structural evolution of sub-cell structure is shown in supplementary Figs. S1(c) and (d).

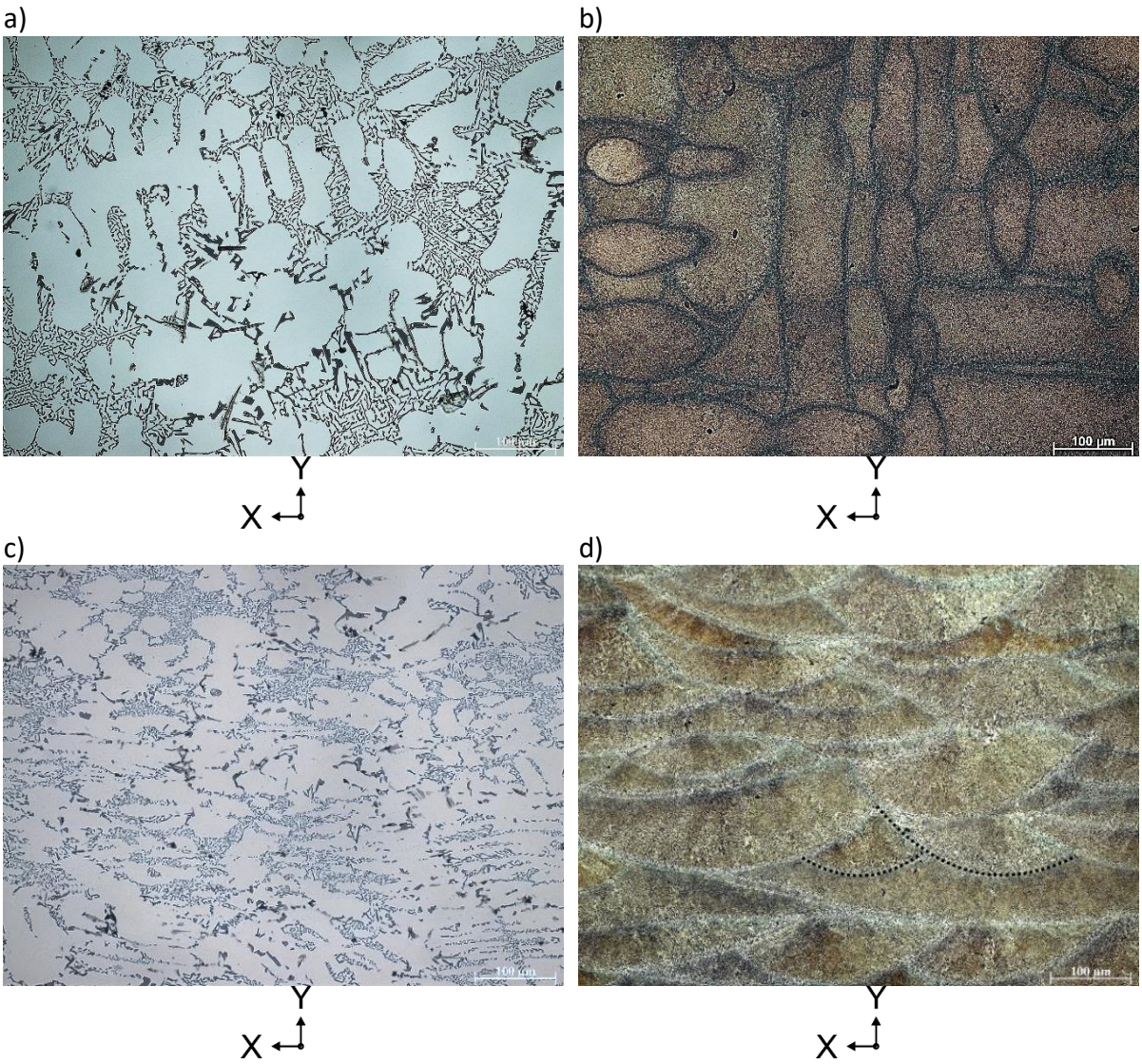

Fig. 8. Light microscopy images of AlSi10Mg alloy a) cast, b) ECAP-processed cast, c) SLM, d) ECAP-processed SLM.

To further investigate the microstructural differences between the ECAP-processed specimens, EBSD analysis was performed (Fig. 9). The image quality (IQ) map of the ECAP-processed cast specimen (Fig. 9(a)) shows the presence of dislocation channels, which appear as dark lines with a reduced IQ. The occurrence of these black areas is most pronounced in the eutectic region. A low IQ value indicates a lower quality of the diffraction pattern, which is influenced by the degree of deformation (regions that experience non-uniform deformation often show lower IQ values). Based on the observed morphology and brightness of the phases, it can be concluded that the dark grey areas in the image represent α-Al corresponding to the matrix of the alloy. On the other hand, the bright areas are indicative of Si rich particles, which are clearly indicated by white arrows. The IQ map shows that fine equiaxed aluminium grains

tend to nucleate in close proximity to these Si particles, indicating a strong localization of dynamic recrystallization (DRX) by a particle-stimulated nucleation (PSN) mechanism [35]. This result is consistent with the observed behaviour of the force-displacement curve (Fig. 4(a)) [36].

Figure 9(b) displays the IQ map of the ECAP-processed SLM specimen. The image demonstrates comparable band contrasts in the coarse-grained region for both the ECAP-processed cast and ECAP-processed SLM specimens. However, noticeably darker contrasts are observed primarily in regions with significant grain refinement. These contrasting areas correspond to the heat-affected zones (HAZs), which exhibit higher ductility and consequently undergo more deformation compared to the surrounding region.

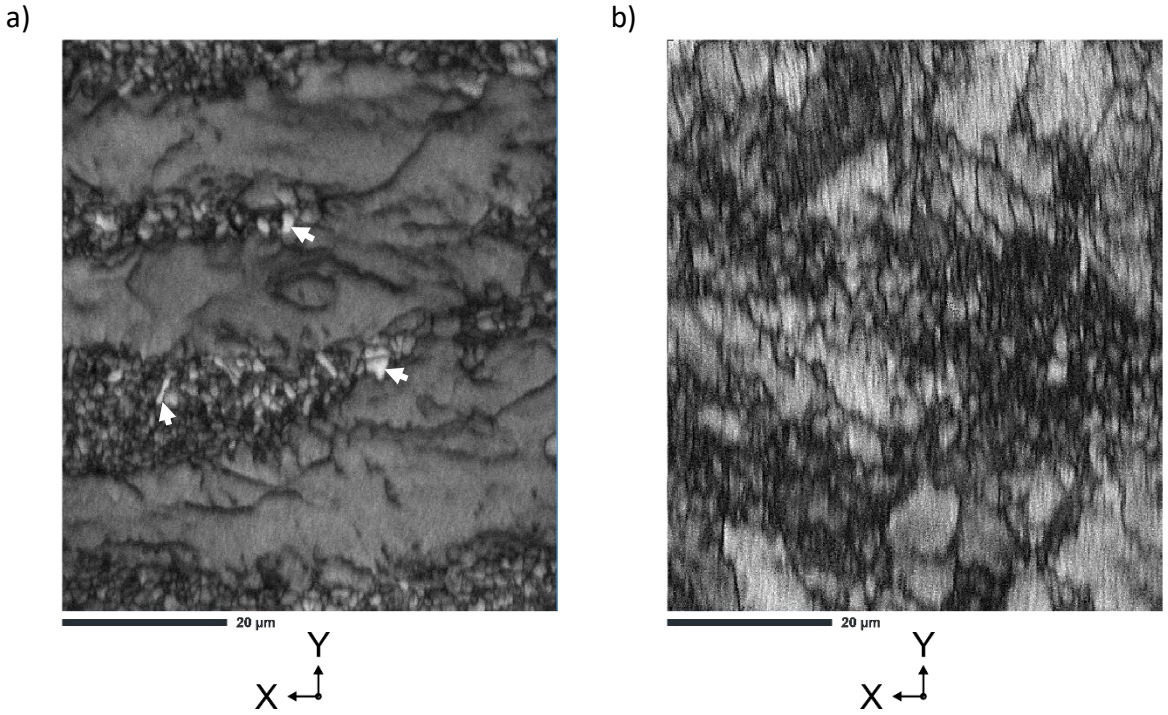

Fig. 9. IQ maps of the AlSi10Mg alloy a) ECAP-processed cast specimen, b) ECAP-processed SLM specimen. Map size is 60 x 70 µm. EBSD scans were taken in the middle of the sample's cross-sections.

Figure 10 shows the IPF-Z maps of the tested specimens. The different colours in the figure represent different grain orientations, as indicated in the IPF diagram in the lower left corner. Analysing Fig. 10(a), it is clear that the ECAP-processed cast specimen has a predominant blue-purple grain colour, corresponding to the <111> direction (typical for ECAP processed cast aluminium alloys). Table 3 shows that low-angle grain boundaries (LAGBs) constitute to 54.9% of the specimen, while high-angle grain boundaries (HAGBs) constitute 35.1%. LAGBs are

mainly present in the coarse-grained zone, while HAGBs are found in the fine-grained (DRX) zone. This observation supports the assumption that Si particles have a positive influence on the grain refinement process by serving as additional nucleation sites for dynamic recrystallization [37]. The measured average grain size of the ECAP-processed cast specimen is 2.5 µm.

Figure 10(b) shows the IPF-Z map of the SLM ECAP-processed counterpart. The grain colour in this case is mainly green and red, which corresponds to the <101> and <001> directions. Similar to the ECAP-processed cast specimen, the LAGBs separate mainly coarse grains, while the HAGBs define fine equiaxed grains. These small subgrains are mainly distributed along the boundaries of the molten pool, resulting in a typical bimodal microstructure. It is noteworthy that the ratio of LAGBs to HAGBs is significantly different from that of the cast counterpart. In the SLM ECAP-processed specimen, HAGBs account for 66.7% of the specimen, while LAGBs account for 33.3%. Also the measured average grain size of ECAP-processed SLM specimen is lower ~ 1.1 µm.

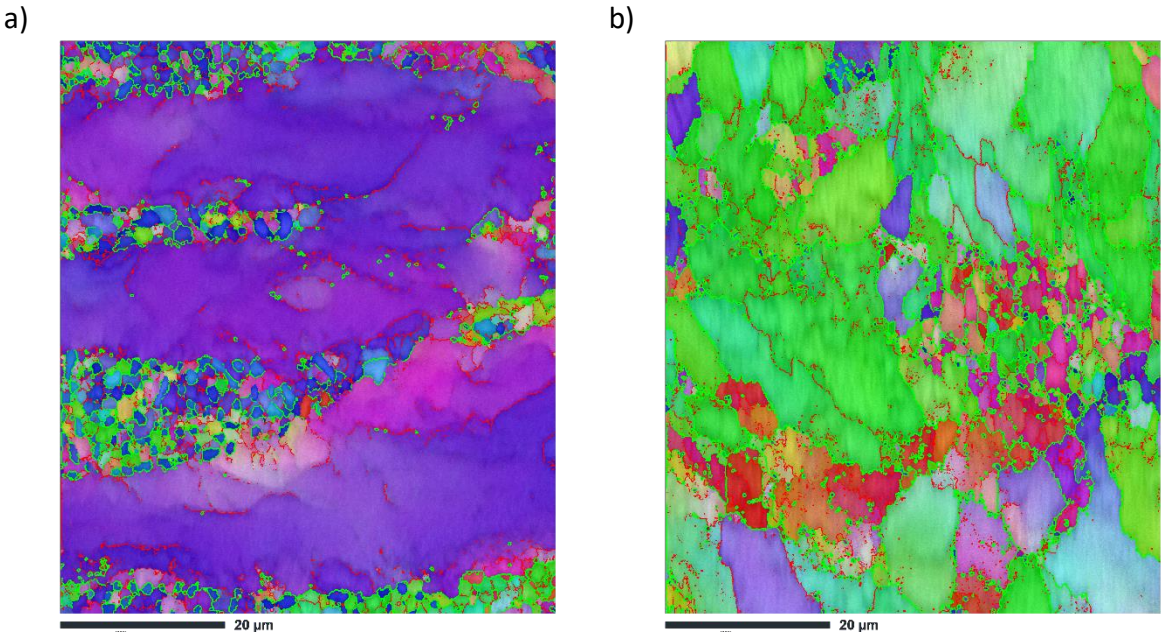

Fig. 10. Coloured inverse pole figure (IPF-Z) maps obtained from EBSD analysis showing the microstructure of a) ECAP-processed cast specimen, b) ECAP-processed SLM specimen. The colour corresponds to the crystallographic orientation shown in the standard stereographic triangle (inset). The colour lines denotes grain boundaries, Red – LAGBs and Green – HAGBs.

Table 3. LAGB ($2° \leq \vartheta \leq 15°$), HAGB ($\vartheta \geq 15°$) fraction (%), grain sizes and GNDs density for ECAP processed specimens.

	f_{LAGBs}, %	f_{HAGBs}, %	GNDs, [m^{-2}]	Grain size, [µm] (GTA=2º)
CAST ECAP	54.9	35.1	3.66×10^{14}	2.5
SLM ECAP	33.3	66.7	5.77×10^{14}	1.1

To elucidate the evolution of the substructure and gain insight into the deformation behaviour, geometrically necessary dislocations (GNDs) maps were plotted (see Fig. 11). These maps were generated based on the kernel average misorientation (KAM), which quantifies the local misorientation within the microstructure. Higher KAM values directly correspond to an increased dislocation density and, consequently, a higher degree of deformation (resulting in higher microstrain within the material). In Fig. 11, different colours show the density of GNDs, as explained by the colour code legend. The average value of the GND density is given in Table 2. It is noteworthy that the average GND density in the SLM sample processed by ECAP is much higher than in the cast sample processed by ECAP.

Figure 11(a) shows the GNDs distribution map of the ECAP-processed cast specimen. In general, the hard Si particles and soft Al matrix have different deformation behaviors, which result in plastic strain inhomogeneity. Therefore, the regions around the Si particles have a higher geometrically dislocation density, as indicated by the red "hot spots" in Fig. 11(a). This also suggests that there is a load transfer effect from the Si particles to the surrounding region. The accumulation of GNDs causes long-range internal stress, which produces back-stress (HDI stress) in the Al matrix and forward stress in the eutectic region [38]. On the other hand, the fine-grained region around the Si particles exhibits relatively low GND density. This implies that DRX has occurred in the specimen. Moreover, the GND distribution between coarse and fine grains is uneven, which may be attributed to heterogeneous deformation. The GND distribution map also shows that the GNDs are concentrated at grain boundary interfaces, especially near the LAGBs.

Figure 11(b) shows the GNDs distribution map of the ECAP-processed SLM sample. The ECAP-processed SLM specimen, which has a finer microstructure, has a much higher GND density. Similar to the ECAP-processed cast specimen, there are visible "hot spots" - areas of high GND density in the microstructure. A closer look at the IPF-Z map (Fig. 11(b)) these areas of high GND density are predominantly located near the fine-grained region corresponding to

the heat-affected zones. According to Song et al. [39], the HAZ zone deforms more than the interior of the melt pool (due to lower strength), which is reflected by an increased GNDs accumulation, which are produced to compensate the strain gradient that built-up. Moreover, it can be seen that even larger grains exhibit a relatively high GND density, which is due to GND accumulation at the cellular interface (GNDs accumulate in front of the Al/Si interface).

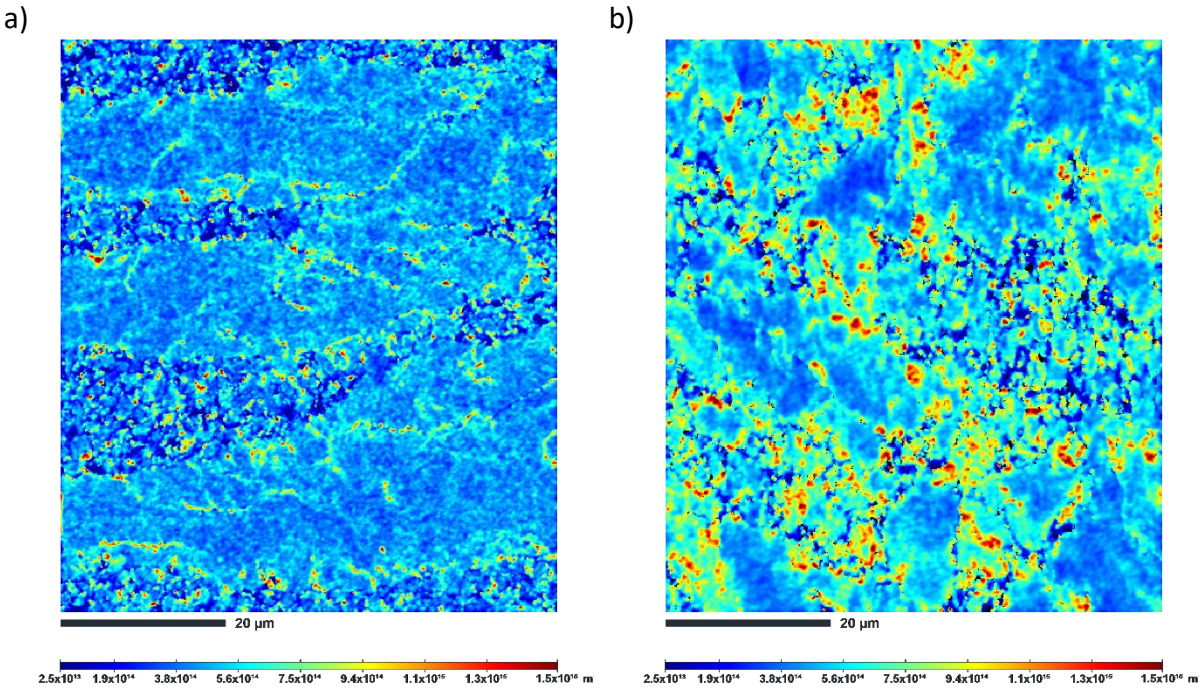

Fig. 11. GNDs maps of the a) ECAP-processed cast specimen, b) ECAP-processed SLM specimen.

The EBSD results show that the subgrain sizes decreased after one ECAP pass for both cast and SLM specimens. They also reveal that the final subgrain size depends on the initial microstructure of the alloy. According to Table 3, the average grain size of the ECAP-processed specimens is 2.5 µm (cast) and 1.1 µm (SLM). This difference in subgrain size after ECAP processing was due to the unique microstructural characteristics of the SLM specimen. This sample had a heterogeneous cellular microstructure; therefore, during ECAP processing the Al/Si interfaces acted as barriers to dislocation slip, leading to a very rapid accumulation of SSDs and GNDs [40]. This dislocation accumulation accelerated the refinement of the cell blocks (after the ECAP process, new sub-grains formed at pre-existing grain boundaries), leading to the formation of dynamically recovered subgrains [41] with low misorientation angles. Since the yield stress of a material is inversely proportional to the square root of the grain size, a smaller subgrain size leads to a higher strength, which is confirmed experimentally in Subchapter 3.3.

3.2. Optical 3D scanning and µCT porosity measurements

Figure 12 presents the results of the optical 3D scanning of the ECAP processed specimens. It is evident that the cast specimen exhibits poorer workability, which led to the formation of significant cracks during ECAP processing. These cracks align along the shear stress direction and are observed on the outer surface of the specimen. In contrast, the SLM specimen has a smooth surface with only a few minor cracks visible

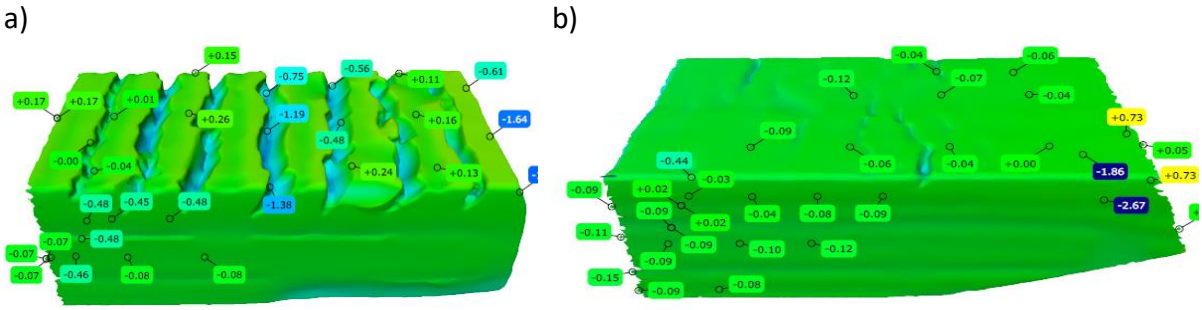

Fig. 12. The results of 3D optical scanning tests a) ECAP-processed cast specimen, b) ECAP-processed SLM specimen.

Figure 13 presents the results of the porosity analysis. The accompanying images show a view of the reconstructed 3D object accompanied by a translucent image highlighting the results of the porosity analysis. The analysis focuses primarily on assessing pore size. Each identified defect is assigned a specific colour based on a predefined scale, which can be used to determine its size.

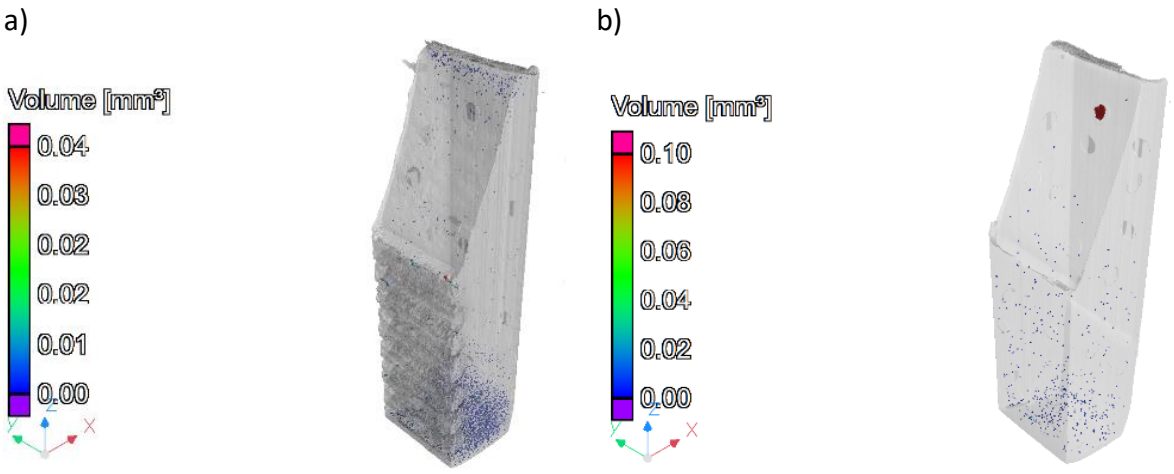

Fig. 13. The results of the porosity measurement a) ECAP-processed cast specimen, b) ECAP-processed SLM specimen.

In Figure 13(a), it is evident that the ECAP-processed cast specimen has a higher number of uniformly distributed defects. The total porosity is determined to be 0.11%, corresponding to approximately 7000 pores. These defects have high sphericity and are predominantly visible at a distance of about 2 mm from the front edge of the ECAP-processed specimen (which experienced less deformation). The µCT scan confirms that the residual pores formed during casting were not completely closed by the ECAP processing (see Supplementary Figure S2).

The ECAP-processed SLM specimen shows a lower porosity compared to its ECAP-processed cast counterpart. It is noticeable that defects are uniformly distributed throughout the specimen. The total porosity is determined to be 0.01%, corresponding to approximately 500 pores.

As observed in both analysed cases, there was a substantial decrease in porosity. This phenomenon can be explained by the favourable stress conditions experienced during ECAP, which ultimately resulted in the closure or minimization of pore geometrical dimensions.

3.3. In-situ tensile µCt studies

In the subsequent phase of our investigation, we conducted in-situ tensile µCT analysis to examine the fracture and mechanical behaviour of both ECAP-processed specimens. For this analysis, we carefully cut specimens from the midsection of the extruded ECAP billet, which displayed a relatively uniform distribution of porosity. The test involved performing scans at a tensile force loads corresponding to the characteristic stress drops observed on the stress-strain curve, Fig. 14.

As can be seen, the microstructural changes (discussed in Subchapter 3.1) have a significant impact on the mechanical perfomance. The most remarkable observation is the substantial increase in tensile strength achieved through the ECAP process. Specifically, the ECAP-processed cast specimen fractures at approximately 175 MPa and true strain of ~0.04, whereas the ECAP-processed SLM specimen fractures at around 370 MPa. Additionally, the SLM specimen fractures at significantly higher true strain value of ~0.12. These findings are noteworthy because such microstructural changes (reduction in grain size) typically result in improved strength, as predicted by the Hall-Petch relationship, which is often achieved at the expense of ductility. Referring to the ECAP-processed SLM alloy, the increased ductility can be attributed to two main microstructural features. The first is the unique multi-level heterogeneous microstructure, which contributes to exceptional mechanical properties, in particular improved work hardening capability. The second is the Si morphology. As can be

seen in Fig. S1, the morphology of the Si precipitates has changed after ECAP processing. For example, in the as-cast sample, the Si size decreased from ~20 µm to ~8 µm. However, in the SLM alloy, the evolution of Si morphology was different. As shown in Fig. S1(c) and (d), ECAP treatment at 300 ºC led to a breakdown and coarsening of the eutectic Si network. According to the study by Li et al [42], the partial discontinuity of the Si network allows the dislocations to penetrate and traverse through the cell boundaries more easily; therefore, the dislocations can move easily on the slip planes, which in turn affects the ductility. In addition, the modified morphology of the Si particles can reduce the stress concentration, which leads to an improvement in elongation at break [43].

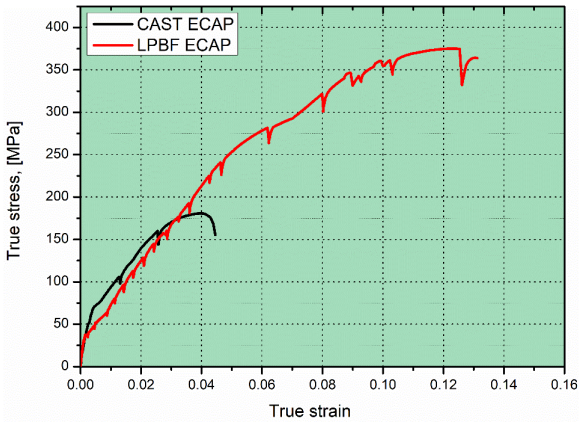

Fig. 14. Stress-strain curve registered during an in-situ µCT analysis.

Figure 15 shows selected 2D µCT slices acquired during the uniaxial in situ tensile test. The µCT scans were performed in the initial condition and at different tensile force loads, which is indicated in each reconstructed image.

Figure 15(a) shows a 2D µCT slice of the ECAP-processed cast specimen before tensile testing. It reveals small spherical void in the reduction area of the tensile specimen (indicated by an arrow). In the first unloaded reconstruction (Fig. 15 (b)), this void is still visible and there is no visible change in the specimen dimensions as a result of applied tensile force. However, in the second reconstruction (Fig. 15 (c)), a slight elongation and reduction of the cross-section can be seen, along with the formation of the first crack network indicated by the yellow arrow. Eventually, the crack expanded (Fig. 15(d)), leading to failure of the specimen due to increasing shear stress. It should be mentioned that the fracture path clearly follows the path from the first crack through the pore that was visible before the fracture. It can be concluded that the failure mechanism of ECAP-processed cast specimens is related to the initial structural features. The presence of defects affects the fracture strength and failure mode.

Figure 15(i) shows the 2D µCT slice of the ECAP-processed SLM specimen before tensile testing. This image clearly shows that the specimen has no pores and voids, which is consistent with the µCT analysis giving a porosity of 0.01%. In the first unloaded reconstruction (Fig. 15 (j)), there are no visible changes in the specimen dimensions. However, in the second reconstruction (Fig. 15 (k)), a more elongation and reduction of the cross-section, can be seen, along with the formation of the first crack network, indicated by the yellow arrow. Finally, the crack expanded (Fig. 15(l)), leading to failure of the specimen due to the increasing shear stress.

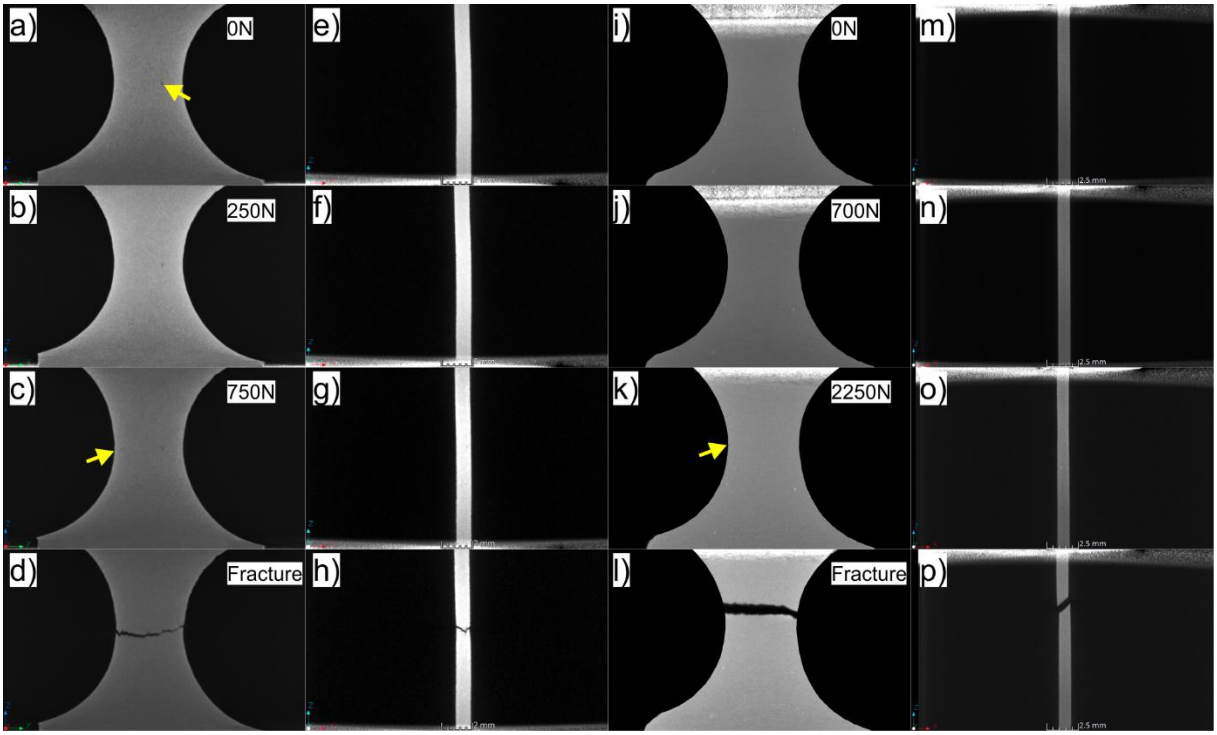

Fig. 15. Selected 2D µCT slices acquired during the in-situ uniaxial tensile test corresponding to the points highlighted in the tensile curves a) ECAP-processed cast, b) ECAP-processed SLM.

In the literature, there are experimental results that focus on the effect of internal defects on the tensile properties of AlSi10Mg alloy produced via SLM. For example, Wu et al. [44] used in situ synchrotron radiation X-ray microcomputed tomography to highlight that large, pancake-shaped loss of fusion (LOF) defects, which are perpendicular to the build direction, significantly affect the material's ductility and failure mode. They revealed that LOF defects can lead to a brittle failure when aligned with the tensile load, while a ductile cup-cone failure occurs when they are perpendicular to it. Moreover, the authors concluded that minimizing the size and aspect ratio of defects is crucial for enhancing the tensile ductility of AlSi10Mg

alloy. In another paper [45], the authors examined how these metallurgical defects affect the fatigue resistance of additively manufactured parts made from AlSi10Mg alloy. Using X-ray computed tomography (CT) to characterize defects, they correlated internal defects with the tensile and high cycle fatigue (HCF) properties of specimens. They found out that despite similar tensile strengths, specimens tested perpendicular to the build direction showed higher elongation and fatigue strength compared to those tested parallel to it. Moreover, the authors of the manuscript revealed that near-surface defects are the primary sites for fatigue crack initiation. The above-mentioned papers highlight the importance of defect reduction and its influence on the tensile properties of SLM AlSi10Mg alloy, and emphasize the importance of defect reduction through the AM process optimization. While these studies focus on as-built samples, our study shows that there are also other opportunities and possibilities for the defect density reduction in SLM samples, such as SPD post-processing, which eliminated the porosity level up to 0.01%, resulting in superior mechanical properties, as revealed by in situ μCT investigation.

3.4. Characterisation of fracture mechanisms

To clarify the differences in failure modes between the ECAP-processed specimens, we performed a thorough analysis of the fracture surfaces. First, the 3D scans of the fracture surfaces were acquired. Our approach was to introduce a theoretical horizontal plane in the cross-section of each specimen where no destruction was observed. This horizontal cross-section had no significant shape changes due to fracture, and we refer to these theoretical planes as the ideal fracture surface in the assumed cross-section.

Figures 16(a) and 16(b) provide a mapped distribution of the distances of the points from the assumed theoretical plane. For the ECAP-processed SLM specimen, a relatively uniform increase in distance was observed. Further examination of the vertical cross-section (Fig. 16(c)) revealed that fracture occurred an angle of 42 degrees.

In contrast, examination of the ECAP-processed cast specimen revealed irregular fracture, and we noted a distinct wedge shape, Fig. 16(b). The separation planes in this case were oriented at 61 degrees and 39 degrees. The cross-section of the ECAP-processed cast is shown in Fig. 16(d).

In the scans, we observed that the ECAP-processed SLM specimen did not show any signs of fracture beyond the separation surface. However, in contrast, the ECAP-processed cast

specimen displayed multiple cracks within its internal structure. These cracks were visible at the edge (Figure 16(d)) and marked with white arrows, suggesting a higher level of brittleness compared to the ECAP-processed SLM specimen.

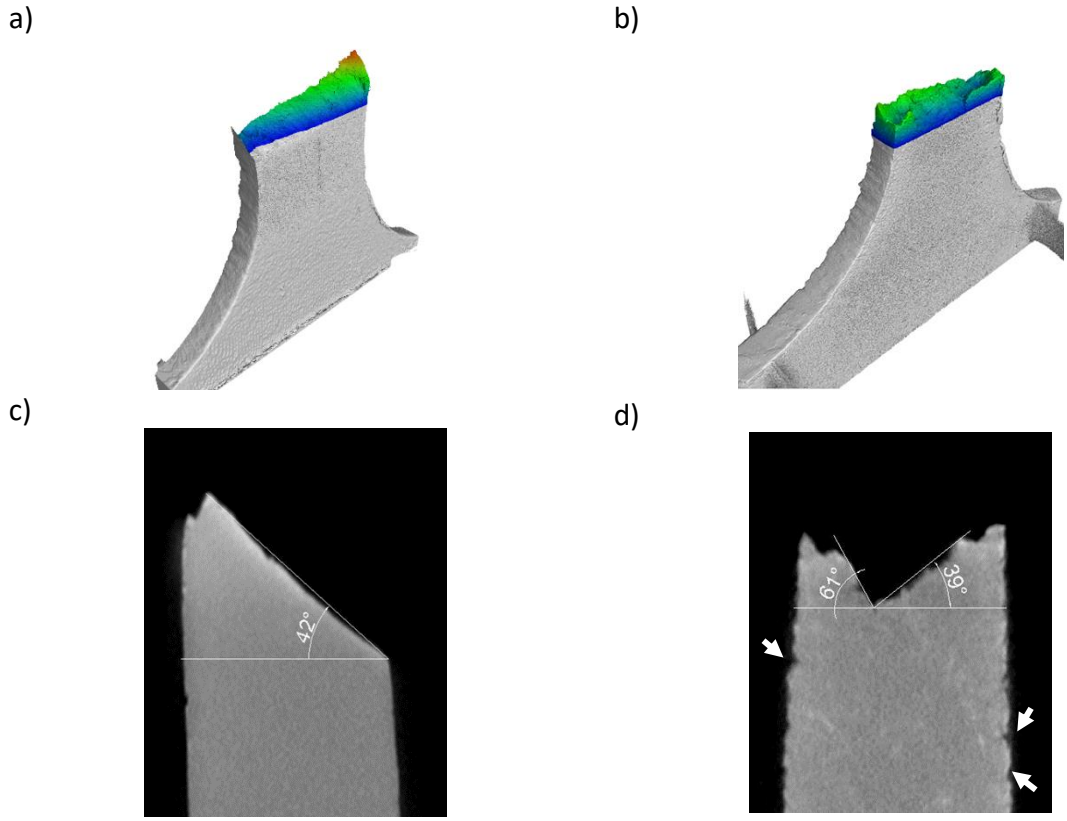

Fig. 16. Tomographic data - surfaces of in-situ damaged ECAP-processed specimens: a) 3D view of ECAP-processed SLM specimen, b) 3D view of ECAP-processed cast specimen, c) section through ECAP-processed SLM specimen, d) ECAP-processed cast specimen.

To gain insight into the failure modes of the ECAP-processed samples, a detailed analysis of the microstructure was carried out by imaging and examining the cross section along the tensile direction near the fracture surface, Fig. 17. As can be seen, the fracture surface of the ECAP-processed cast specimen exhibits well-defined cleavage planes, accompanied by raised features that resemble hills. The fracture path follows the acicular eutectic silicon particles (ESPs) and dendrite boundaries, as depicted in Figure 17(a). This occurrence can be attributed to the weak zone formed at the matrix/particle interfaces, where the sharp edges of the particles serve as potential sites for crack initiation [46]. Moreover, the image highlights several cracked eutectic Si particles, indicated by white arrows. These cracks clearly result from the tensile force, since no cracks were detected in this specimen prior to the tensile test.

Figure 17(b) shows the fracture path of ECAP-processed SLM specimen is much smoother than that of the ECAP-processed cast counterpart. From this image, it is also evident that the crack path preferentially follows weaker zones, which have much lower yield strength and hardness. In case of ECAP-processed SLM specimen this is a heat-affected zone, where thermal variations and repeated remelting during the SLM process lead to a coarsening of the microstructural features, namely the eutectic α-Al and Si zones. This coarser microstructure exhibits lower yield strength and hardness due to reduced grain boundary strengthening, as shown by the Hall-Petch relationship [47]. It is worth noting that in previous studies on SLM Al-SI alloys, similar fracture behaviour was observed, which means that the ECAP process did not affect the fracture mode significantly [48]

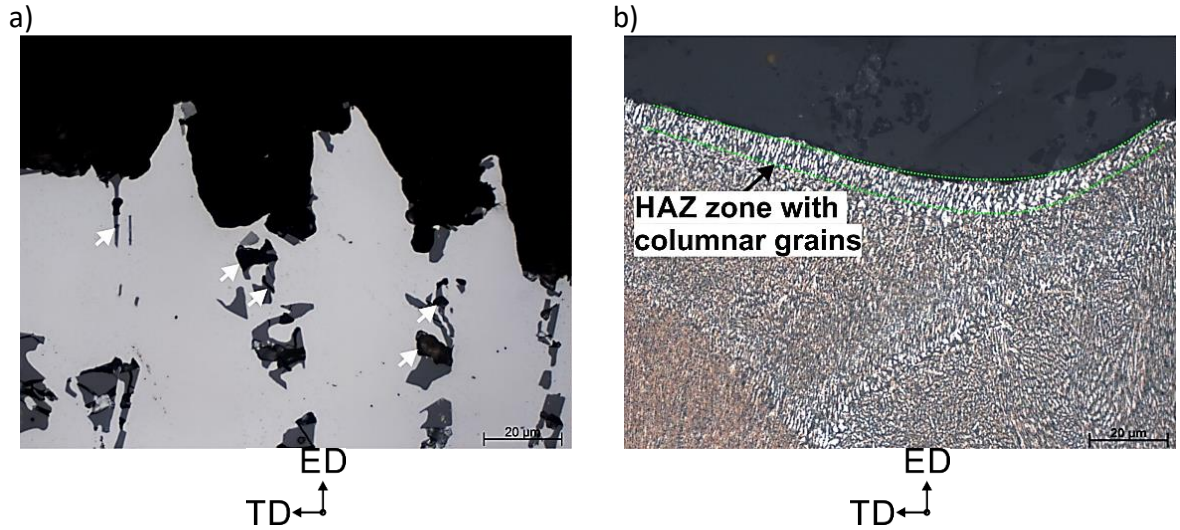

Fig. 17. Light microscopy images of the fractured region a) ECAP-processed cast specimen, b) ECAP-processed SLM specimen.

In the next stage of the investigation, the fracture surfaces of the deformed tensile specimens were comprehensively examined in a scanning electron microscope. Figure 18 shows the SEM images taken at three different magnification levels. A clear distinction can be observed between the fracture surface of the ECAP-processed cast specimen and that of the ECAP-processed SLM counterpart. As mentioned earlier, the ECAP-processed cast specimen lacked distinct necking fracture features, which indicated its comparatively poorer tensile ductility (see Fig. 15). This is reflected in a mixed fracture mode, characterized by the presence of small dimples (<10 µm) across the fracture surface, which indicate plastic deformation of the aluminium matrix [49]. Additionally, Fig. 18(c) reveals the origin of cracks from the brittle fracture of the primary Si particles. It can be concluded that, during tensile testing, cracks

typically propagate along these brittle Si phases and interdendritic regions. During tensile loading, the aluminium matrix provides additional ductility, while the brittle fracture mode of the Si phase and its detachment from the alloy matrix (as seen in Fig. 18(e)) result in a more rapid fracture, thus limiting the elongation at fracture of the ECAP-processed cast specimen. The general fracture morphology aligns with what has been reported in the literature for Al-Si cast alloys [28,50,51].

The fracture surface of the ECAP-processed SLM specimen, Fig. 18, consists of dimples and tear edges, confirming its well ductility. It is also evident from Fig. 18(b) that failure occurs along the HAZ, which are dominated by the larger Si particles and cells. These coarse and brittle particles have the potential to facilitate damage progression. On closer examination in Figs. 18(d) and (f), the fracture surface shows shallow, minuscule dimples (< 1 μm) that are similar in size to Si cells. This suggests that the fracture occurred as a result of the detachment of soft Al cells from the edges of the hard eutectic-Si network. Interestingly, no porosity or voids were detected on the fracture surface, which could have served as crack initiation sites. This finding is consistent with the μCT analysis and confirms that the ECAP processing effectively eliminated any remaining porosity in the SLM specimens.

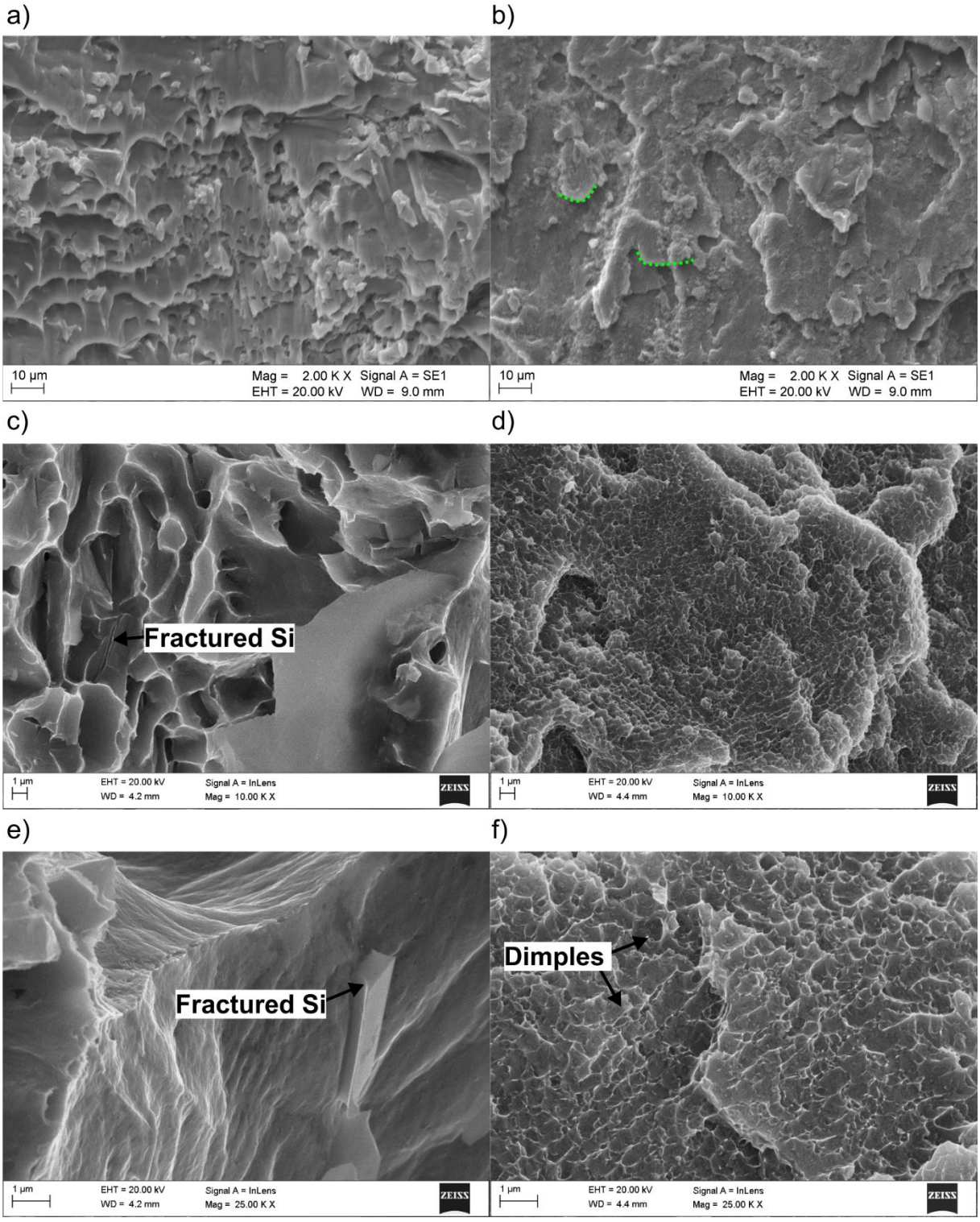

Fig. 18. Fracture surfaces of ECAP processed specimens (a),(c), (e), cast and (b),(d),(f), SLM with increasing magnification.

To shed light on the physical nature of the strain-hardening mechanisms, cyclic straining was done by performing several loading unload–reload cycles with increasing unloading strain, up to fracture, Figure 19. Notably, the hysteresis loops recur in each cycle, indicating

the presence of the Bauschinger effect. However, the ECAP-processed SLM alloy exhibits a larger hysteresis loop during the unloading-reloading cycle, indicating a stronger hetero-deformation induced stress (σ_{HDI}) which can be expressed using the following equation:

$$\Delta\sigma_{HDI} = \frac{\sigma_{r+}\sigma_u}{2} \quad (1)$$

Where:

σ_u and σ_r are unloading yield stress and reloading yield stress, respectively.

From Fig. 19(a) it is also evident that the HDI stress increases as the strain rises. Furthermore, the HDI stresses are significantly higher for the ECAP-processed SLM specimen, accounting for nearly 55% of the yield stress, Fig. 19(c). The amplified HDI stresses in the ECAP-processed SLM specimen can be attributed to its distinctive multilevel heterogeneous microstructure, that is composed of heat-affected zones, bimodal grains and cellular network [52]. During tensile deformation, the HAZs experience more deformation than that melt pool interior, hence a plastic strain gradient builds up. This incompatibility is compensated by geometrically necessary dislocations. Furthermore, the hard Si network restricts the deformation of the soft Al matrix, resulting in a strain gradient (i.e., geometrically necessary dislocations) near the Al-Si interface during plastic deformation, activating HDI stresses [42,53].

Assuming that ρ_{GND} is proportional to the strain gradient i.e., the variation of plastic strain over the microstructural length (λ) for which the gradient is generated (λ can be taken as the mean spacing between Si particles in the eutectic zone ~ 1500 nm, while for SLM ECAP specimen, λ value can be taken as the average cell size ~ 400 nm); Equation 2, where ε is the applied strain and b is the length of the Burgers vector (Al = 0.286 nm), it is reasonable to anticipate higher HDI stress and GND density in the ECAP-processed SLM specimen.

$$\rho_{GND} = \frac{8\varepsilon}{3b\lambda} \quad (2)$$

This is because the average distance travelled by geometrically necessary dislocations is shorter in an SLM specimen. In other words, when the gradient is created on a smaller microstructural length (λ), it leads to a higher accumulation of GNDs during plastic deformation [54]. These assumptions align with the EBSD analysis presented in subchapter 3.1, which revealed a significantly higher density of GNDs for the ECAP-processed SLM specimen. Similar findings have also been reported by Li et al. [55] in their work on SLM

AlSi10Mg showing that cellular dislocation structure contributes significantly to the hetero-deformation induced (HDI) stress.

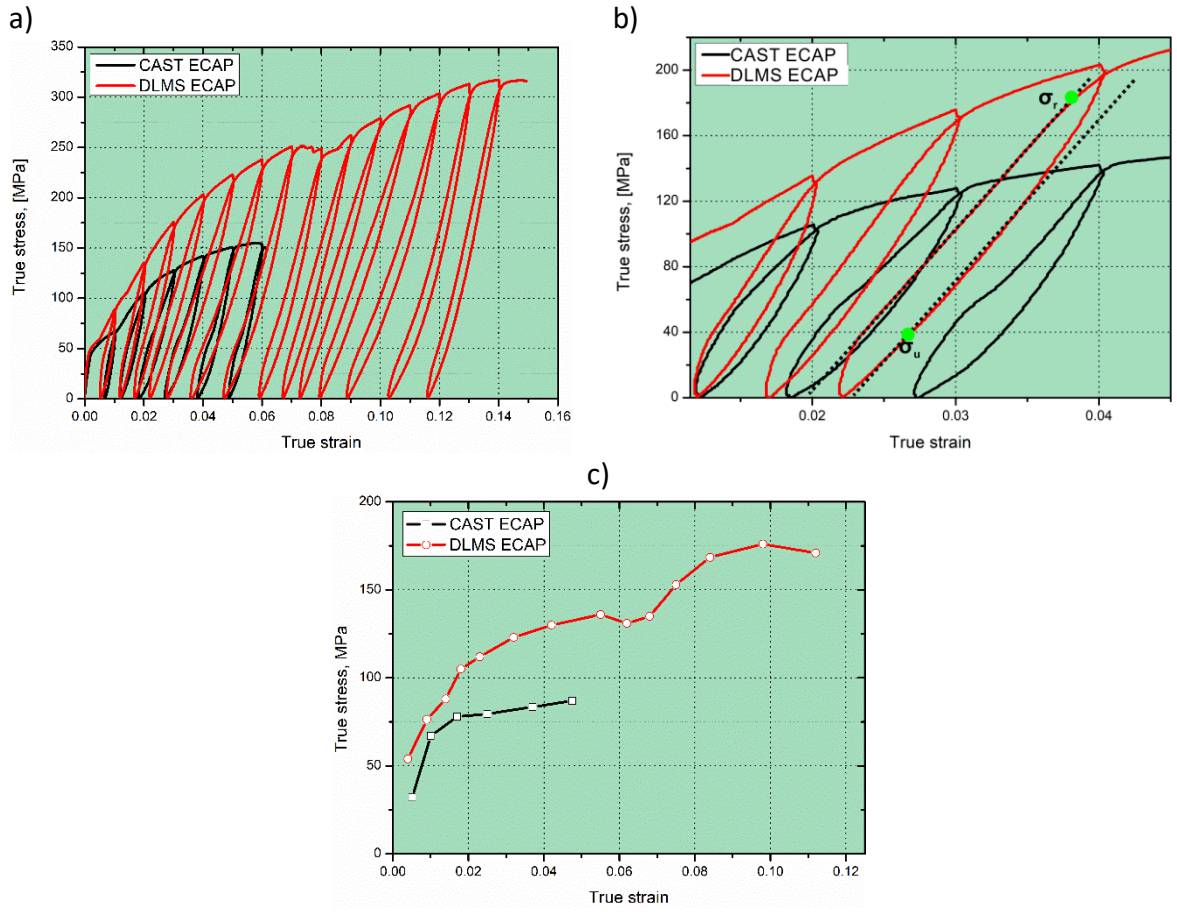

Fig. 19 (a) LUR curves of the ECAP processed specimens. (b) schematic of an unloading-reloading loop (c) Evolution of HDI stress as a function of true strain deduced from the LUR curves.

The microstructural characteristics induced by tensile deformation were further investigated by EBSD, and the corresponding results are shown in Figure 20. The areas selected for the EBSD analysis were approximately 20 µm from the fracture surface. Figure 20(a) shows an IQ map obtained from the EBSD scan, which clearly highlights black areas indicating the absence of signal. The presence of unidentified areas near the fracture surface suggests the existence of porosity, which has formed as a result of silicon detachment from the aluminium matrix under the influence of the applied tensile force (note that the green dashed lines outline the Si precipitates).

Figure 20(c) shows the geometrically necessary distribution map of the ECAP-processed cast specimen. Interestingly, the analysis reveals that the local orientation gradients within

the grains are slightly lower in the tensile tested specimen (ρ_{GND}=5.62×$10^{14}$$m^{-2}$) than in an undeformed counterpart (ρ_{GND}=3.58×$10^{14}$$m^{-2}$). However, the results are affected by several unidentified areas with zero GND density. It is also observed that the increased localised lattice distortion predominantly starts from the hard particles and grain boundaries (the grain boundaries are visible as thin white lines in the GND map), thereby confirming the presence of strain heterogeneity distribution detected via LUR tests.

Figure 20(b) presents an IQ map of the tensile-tested ECAP-processed SLM specimen. Compared to the undeformed specimen, one can see that multiple subgrains formed during the test. These subgrains are characterised by a darker contrast at their boundaries, indicating lower image quality values or a greater degree of lattice distortion, which can be attributed to localised deformation processes. The size of the subgrain is similar to that of Si cells, suggesting a correlation between the subgrain formation and the initial microstructure of the material.

Figure 20(d) shows the geometrically necessary distribution map of the ECAP-processed cast specimen. The average ρ_{GND} value is 5.06×$10^{14}$$m^{-2}$, which is similar to that of the ECAP-processed SLM specimen prior to the tensile test. This indicates that GNDs slightly decreased after fracture, possibly due to stress relaxation near the fracture surface caused by the annihilation and rearrangement of the dislocations. Moreover, it is important to note that the crack tip can experience more localised plastic deformation [56], which may generate new dislocations and increase the density of GND in those specific regions. However, this study did not analyse this particular region.

In addition to the effect of high ρ_{GND} in the ECAP-processed SLM specimen, the distribution of the dislocation also has a great influence on the material ductility. As can be seen in Fig. 20(d), the GNDs are heterogeneously distributed within the subgrains. Hence, it is not surprising to see that some of the fine grains carry very low strain gradients, i.e., low GND density. This heterogeneous distribution of GNDs potentially correlates to HDI stress generated in this unique microstructure, as revealed by the LUR tests.

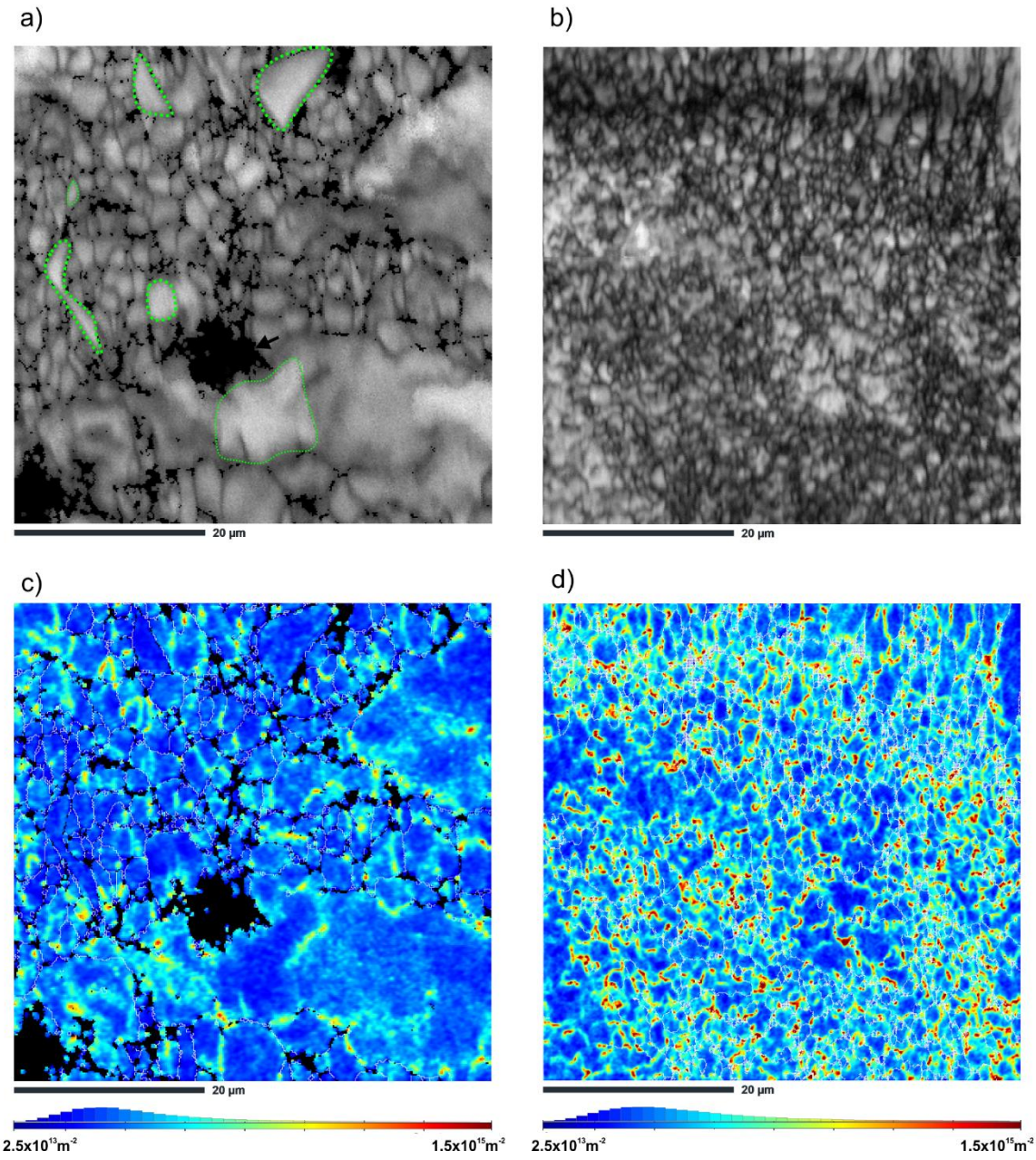

Fig. 20. Result of the EBSD analysis of the fractured specimens a) IQ map of ECAP-processed cast specimen, b) IQ map of DLSM ECAP-processed specimen, c) GNDs map of ECAP-processed cast specimen, d) GNDs map of ECAP-processed SLM specimen.

Conclusions

This paper comprehensively examines the microstructure, mechanical properties, and fracture characteristics of ECAP-processed cast and SLM AlSi10Mg alloy, shedding light on the resulting structure-property relationships. The main findings can be summarized as follows:

- Specimens after ECAP have higher density than before, which is due to the reduction in porosity after ECAP.

- ECAP processing results in the breakage of the eutectic silicon particles and refinement of the aluminium matrix. Particle fragmentation occurs in response to large stresses associated with processing to substantial strains at elevated temperatures. Specifically, it is revealed that particle-stimulated nucleation plays a crucial role in achieving efficient grain refinement in cast specimen. After one ECAP pass, the grain size was reduced to around 2.5 μm.
- A remarkable refinement of the microstructure down to the ultrafine grain regime was achieved. According to EBSD analysis, the microstructure of ECAP-processed SLM specimen consists of subgrains with an average size of ~1.1 μm.
- ECAP treatment results in partial fragmentation and coarsening of the eutectic Si network in SLM specimen, which made the movement of dislocation easier through the substructure.
- The generation and storage of geometrically necessary dislocations (GNDs) in the ECAP-processed SLM specimen is promoted by the strain partitioning between Al/Si cellular domains during tensile deformation.
- The tensile behaviour of ECAP-processed cast and SLM specimens exhibits significant differences. Specifically, the ECAP-processed SLM specimen shows a 50% higher tensile strength compared to its ECAP-processed cast counterpart. Tensile strength of ECAP-processed SLM specimen exceeds 370 MPa with a total strain at fracture over 12 %.
- The loading-unloading-reloading tests reveal that the HDI stress induces extra strain hardening. The HDI stress contributes to about 50% of global flow stress of the ECAP-processed SLM sample.
- The main crack propagation of ECAP-processed cast specimen is along the acicular eutectic silicon particles (ESPs) and dendrite boundaries; whereas, in the case of the ECAP-processed SLM specimen, the fracture occurs predominantly along the softer heat-affected zones.
- Fracture surface morphologies studied by SEM provided valuable insights into the crack origin. The primary factor contributing to premature fracture in the ECAP-processed cast sample is the weak bonding between the aluminium and ESPs, which playes a major role in the creation and propagation of cracks.

- The finer microstructure of ECAP-processed SLM sample is less prone to fracture, forming small dimples associated with the detachment of Al cells from the Si eutectic network.
- ECAP demonstrates remarkable potential as a processing tool for achieving nearly complete elimination of porosity in 3D printed metallic specimens, leading to a significant improvement in mechanical response. The μCt studies revealed that a single ECAP pass resulted in total porosity of only 0.11% and 0.01% for the cast and SLM ECAP-processed specimens, respectively.

This comparative study not only provided valuable insights into the fracture mechanisms, crack initiation and propagation pathways, but also contributed to a deeper understanding of the unique mechanical responses observed in different ECAP-processed AlSi10Mg alloy samples. The results highlight the influence of the initial material state on the resulting mechanical properties paving the way for improved material selection and processing techniques in engineering applications requiring higher performance and structural durability.

Funding

The research was funded by the National Science Centre, Poland based on the decision number 2021/43/D/ST8/01946.

References

[1] Gradl P, Tinker DC, Park A, Mireles OR, Garcia M, Wilkerson R, et al. Robust Metal Additive Manufacturing Process Selection and Development for Aerospace Components. J Mater Eng Perform 2022;31:6013–44. https://doi.org/10.1007/s11665-022-06850-0.

[2] Wu Z, Wu S, Qian W, Zhang H, Zhu H, Chen Q, et al. Structural integrity issues of additively manufactured railway components: Progress and challenges. Eng Fail Anal 2023;149:107265. https://doi.org/https://doi.org/10.1016/j.engfailanal.2023.107265.

[3] Bharath C, Shamanth V, Hemanth K. Studies on mechanical behaviour of AlSi10Mg alloy produced by Selective Laser Melting and A360 alloy by die casting. Mater Today Proc 2021;45:78–81. https://doi.org/10.1016/J.MATPR.2020.10.095.

[4] Sathishkumar A, Soundararajan R, Sivasankaran S. Effect of Direct Aging on the Microstructure and Mechanical Behavior of AlSi10Mg Alloy: Casting Versus Selective Laser Melting. J Mater Eng Perform 2023;32:3215–29.

https://doi.org/10.1007/s11665-022-07315-0.

[5] Pereira JC, Gil E, Solaberrieta L, San Sebastián M, Bilbao Y, Rodríguez PP. Comparison of AlSi7Mg0.6 alloy obtained by selective laser melting and investment casting processes: Microstructure and mechanical properties in as-built/as-cast and heat-treated conditions. Mater Sci Eng A 2020;778:139124. https://doi.org/10.1016/J.MSEA.2020.139124.

[6] Shakil SI, Hadadzadeh A, Shalchi Amirkhiz B, Pirgazi H, Mohammadi M, Haghshenas M. Additive manufactured versus cast AlSi10Mg alloy: Microstructure and micromechanics. Results Mater 2021;10:100178. https://doi.org/https://doi.org/10.1016/j.rinma.2021.100178.

[7] Yu W, Zhao H, Wang L, Guo Z, Xiong S. The influence of T6 treatment on fracture behavior of hypereutectic Al-Si HPDC casting alloy. J Alloys Compd 2018;731:444–51. https://doi.org/https://doi.org/10.1016/j.jallcom.2017.10.074.

[8] Babapour Golafshani K, Nourouzi S, Jamshidi Aval H. Hot tensile deformation and fracture behavior of friction stir processed Al-Si-Cu alloy. CIRP J Manuf Sci Technol 2021;35:41–52. https://doi.org/https://doi.org/10.1016/j.cirpj.2021.04.008.

[9] Li Y, Yang M, Li K, Ma C, Yang T, Wang J, et al. In-situ study of effects of heat treatments and loading methods on fracture behaviors of a cast Al–Si alloy. Mater Today Commun 2021;28:102680. https://doi.org/https://doi.org/10.1016/j.mtcomm.2021.102680.

[10] Lee C, Shin K, Kim Y. Dependence of tensile ductility on damage evolution of eutectic Si-particles and pre-existing micro-voids in Al-Si casting alloy. Eng Fract Mech 2017;175:339–56. https://doi.org/https://doi.org/10.1016/j.engfracmech.2016.12.014.

[11] Vuksanovic D, Asanovic V, Scepanovic J, Radonjic D. Effect of chemical composition and T6 heat treatment on the mechanical properties and fracture behaviour of Al-Si alloys for IC engine components. J Min Metall Sect B Metall 2021;57:195–207.

[12] Reid TK, Yavas B, Sahoo S, Alpay SP. Topological variations in aluminum-silicon alloys through inoculation with alkali earth elements: A first-principles study. Scr Mater 2023;234:115574. https://doi.org/https://doi.org/10.1016/j.scriptamat.2023.115574.

[13] Cao Y, Chen X, Wang Z, Chen K, Pan S, Zhu Y, et al. Synergistic influence of La and Zr on microstructure and mechanical performance of an Al-Si-Mg alloy at casting state. J

Alloys Compd 2022;902:163829.
https://doi.org/https://doi.org/10.1016/j.jallcom.2022.163829.

[14] Van Cauwenbergh P, Samaee V, Thijs L, Nejezchlebová J, Sedlák P, Iveković A, et al. Unravelling the multi-scale structure–property relationship of laser powder bed fusion processed and heat-treated AlSi10Mg. Sci Rep 2021;11:6423. https://doi.org/10.1038/s41598-021-85047-2.

[15] Hadadzadeh A, Amirkhiz BS, Shakerin S, Kelly J, Li J, Mohammadi M. Microstructural investigation and mechanical behavior of a two-material component fabricated through selective laser melting of AlSi10Mg on an Al-Cu-Ni-Fe-Mg cast alloy substrate. Addit Manuf 2020;31:100937. https://doi.org/https://doi.org/10.1016/j.addma.2019.100937.

[16] Snopiński P, Król M, Pagáč M, Petrů J, Hajnyš J, Mikuszewski T, et al. Effects of equal channel angular pressing and heat treatments on the microstructures and mechanical properties of selective laser melted and cast AlSi10Mg alloys. Arch Civ Mech Eng 2021;21:92. https://doi.org/10.1007/s43452-021-00246-y.

[17] Snopiński P, Hilšer O, Hajnyš J. Tuning the defects density in additively manufactured fcc aluminium alloy via modifying the cellular structure and post-processing deformation. Mater Sci Eng A 2023;865:144605. https://doi.org/https://doi.org/10.1016/j.msea.2023.144605.

[18] Bao J, Wu Z, Wu S, Hu D, Sun W, Wang R. The role of defects on tensile deformation and fracture mechanisms of AM AlSi10Mg alloy at room temperature and 250 °C. Eng Fract Mech 2022;261:108215. https://doi.org/https://doi.org/10.1016/j.engfracmech.2021.108215.

[19] Roth CC, Tancogne-Dejean T, Mohr D. Plasticity and fracture of cast and SLM AlSi10Mg: High-throughput testing and modeling. Addit Manuf 2021;43:101998. https://doi.org/https://doi.org/10.1016/j.addma.2021.101998.

[20] Zhao L, Santos Macías JG, Douillard T, Li Z, Simar A. Unveiling damage sites and fracture path in laser powder bed fusion AlSi10Mg: Comparison between horizontal and vertical loading directions. Mater Sci Eng A 2021;807:140845. https://doi.org/https://doi.org/10.1016/j.msea.2021.140845.

[21] Amir B, Grinberg E, Gale Y, Sadot O, Samuha S. Influences of platform heating and post-processing stress relief treatment on the mechanical properties and

microstructure of selective-laser-melted AlSi10Mg alloys. Mater Sci Eng A 2021;822:141612. https://doi.org/https://doi.org/10.1016/j.msea.2021.141612.

[22] Rosenthal I, Shneck R, Stern A. Heat treatment effect on the mechanical properties and fracture mechanism in AlSi10Mg fabricated by additive manufacturing selective laser melting process. Mater Sci Eng A 2018;729:310–22. https://doi.org/10.1016/J.MSEA.2018.05.074.

[23] Hirata T, Kimura T, Nakamoto T. Effects of hot isostatic pressing and internal porosity on the performance of selective laser melted AlSi10Mg alloys. Mater Sci Eng A 2020. https://doi.org/10.1016/j.msea.2019.138713.

[24] Maleki E, Bagherifard S, Unal O, Jam A, Shao S, Guagliano M, et al. Superior effects of hybrid laser shock peening and ultrasonic nanocrystalline surface modification on fatigue behavior of additive manufactured AlSi10Mg. Surf Coatings Technol 2023;463:129512. https://doi.org/https://doi.org/10.1016/j.surfcoat.2023.129512.

[25] Yusuf SM, Hoegden M, Gao N. Effect of sample orientation on the microstructure and microhardness of additively manufactured AlSi10Mg processed by high-pressure torsion. Int J Adv Manuf Technol 2020. https://doi.org/10.1007/s00170-019-04817-5.

[26] Hosseinzadeh A, Radi A, Richter J, Wegener T, Sajadifar SV, Niendorf T, et al. Severe plastic deformation as a processing tool for strengthening of additive manufactured alloys. J Manuf Process 2021;68:788–95. https://doi.org/10.1016/J.JMAPRO.2021.05.070.

[27] Snopiński P, Matus K, Tatiček F, Rusz S. Overcoming the strength-ductility trade-off in additively manufactured AlSi10Mg alloy by ECAP processing. J Alloys Compd 2022;918:165817. https://doi.org/10.1016/J.JALLCOM.2022.165817.

[28] Damavandi E, Nourouzi S, Rabiee SM, Jamaati R, Szpunar JA. Effect of route BC-ECAP on microstructural evolution and mechanical properties of Al–Si–Cu alloy. J Mater Sci 2021;56:3535–50. https://doi.org/10.1007/s10853-020-05479-5.

[29] Moradi M, Nili-Ahmadabadi M, Heidarian B. Improvement of mechanical properties of AL (A356) cast alloy processed by ECAP with different heat treatments. Int J Mater Form 2009;2:85. https://doi.org/10.1007/s12289-009-0641-3.

[30] Song D, Wang G, Zhou Z, Klu EE, Gao B, Ma A, et al. Developing a high-strength Al–11Si alloy with improved ductility by combining ECAP and cryorolling. Mater Sci Eng A 2020;773:138880. https://doi.org/10.1016/J.MSEA.2019.138880.

[31] Ribeiro AKC, de Freitas RFCP, de Carvalho IHG, de Miranda LM, da Silva NR, de Fátima Dantas de Almeida L, et al. Flexural strength, surface roughness, micro-CT analysis, and microbiological adhesion of a 3D-printed temporary crown material. Clin Oral Investig 2023;27:2207–20. https://doi.org/10.1007/s00784-023-04941-3.

[32] Böhm R, Stiller J, Behnisch T, Zscheyge M, Protz R, Radloff S, et al. A quantitative comparison of the capabilities of in situ computed tomography and conventional computed tomography for damage analysis of composites. Compos Sci Technol 2015;110:62–8. https://doi.org/https://doi.org/10.1016/j.compscitech.2015.01.020.

[33] Leon A, Shirizly A, Aghion E. Corrosion behavior of AlSi10Mg alloy produced by additive manufacturing (AM) vs. Its counterpart gravity cast alloy. Metals (Basel) 2016. https://doi.org/10.3390/met6070148.

[34] Fathi P, Mohammadi M, Duan X, Nasiri AM. A comparative study on corrosion and microstructure of direct metal laser sintered AlSi10Mg_200C and die cast A360.1 aluminum. J Mater Process Technol 2018;259:1–14. https://doi.org/10.1016/J.JMATPROTEC.2018.04.013.

[35] Cho KT, Yoo S, Lim KM, Kim HS, Lee WB. Effect of Si content on surface hardening of Al-Si alloy by shot peening treatment. J. Alloys Compd., 2011. https://doi.org/10.1016/j.jallcom.2011.01.216.

[36] Damavandi E, Nourouzi S, Rabiee SM, Jamaati R, Szpunar JA. EBSD study of the microstructure and texture evolution in an Al–Si–Cu alloy processed by route A ECAP. J Alloys Compd 2021;858:157651. https://doi.org/10.1016/J.JALLCOM.2020.157651.

[37] Ke D, Hengcheng L, Qiumin J, Yun T. Effect of hot extrusion on mechanical properties and microstructure of near eutectic Al-12.0%Si-0.2%Mg alloy. Mater Sci Eng A 2010. https://doi.org/10.1016/j.msea.2010.07.068.

[38] Zhu C, Wang Z, Zhou K, Wu Q, Zhao P, Fan X, et al. Triple the ductility of as-cast Al–Si alloys by phase-selective recrystallization. Mater Sci Eng A 2022;855:143902. https://doi.org/https://doi.org/10.1016/j.msea.2022.143902.

[39] Song L, Zhao L, Ding L, Zhu Y, Huang M, Simar A, et al. Microstructure and loading direction dependent hardening and damage behavior of laser powder bed fusion AlSi10Mg. Mater Sci Eng A 2022;832:142484. https://doi.org/https://doi.org/10.1016/j.msea.2021.142484.

[40] Hadadzadeh A, Baxter C, Amirkhiz BS, Mohammadi M. Strengthening mechanisms in

direct metal laser sintered AlSi10Mg: Comparison between virgin and recycled powders. Addit Manuf 2018;23:108–20. https://doi.org/10.1016/J.ADDMA.2018.07.014.

[41] Wang Y, Zhao Y, Xu X, Pan D, Jiang W, Yang X, et al. Superior mechanical properties induced by the interaction between dislocations and precipitates in the electro-pulsing treated Al-Mg-Si alloys. Mater Sci Eng A 2018;735:154–61. https://doi.org/https://doi.org/10.1016/j.msea.2018.08.029.

[42] Li Z, Li Z, Tan Z, Xiong DB, Guo Q. Stress relaxation and the cellular structure-dependence of plastic deformation in additively manufactured AlSi10Mg alloys. Int J Plast 2020. https://doi.org/10.1016/j.ijplas.2019.12.003.

[43] Zhuo X, Zhang Q, Liu H, Hu Z, Zhang P, Jiang J, et al. Enhanced tensile strength and ductility of an Al-6Si-3Cu alloy processed by room temperature rolling. J Alloys Compd 2022;899:163321. https://doi.org/https://doi.org/10.1016/j.jallcom.2021.163321.

[44] Wu Z, Wu S, Gao X, Lin Y, Xue Y, Withers PJ. The role of internal defects on anisotropic tensile failure of L-PBF AlSi10Mg alloys. Sci Rep 2023;13:14681. https://doi.org/10.1038/s41598-023-39948-z.

[45] Wu Z, Wu S, Bao J, Qian W, Karabal S, Sun W, et al. The effect of defect population on the anisotropic fatigue resistance of AlSi10Mg alloy fabricated by laser powder bed fusion. Int J Fatigue 2021;151:106317. https://doi.org/https://doi.org/10.1016/j.ijfatigue.2021.106317.

[46] Immanuel RJ, Panigrahi SK. Influence of cryorolling on microstructure and mechanical properties of a cast hypoeutectic Al–Si alloy. Mater Sci Eng A 2015;640:424–35. https://doi.org/10.1016/J.MSEA.2015.06.019.

[47] Maconachie T, Leary M, Zhang J, Medvedev A, Sarker A, Ruan D, et al. Effect of build orientation on the quasi-static and dynamic response of SLM AlSi10Mg. Mater Sci Eng A 2020;788:139445. https://doi.org/https://doi.org/10.1016/j.msea.2020.139445.

[48] Patakham U, Palasay A, Wila P, Tongsri R. MPB characteristics and Si morphologies on mechanical properties and fracture behavior of SLM AlSi10Mg. Mater Sci Eng A 2021;821:141602. https://doi.org/10.1016/J.MSEA.2021.141602.

[49] Zhang K, Yu H, Liu J, Li Y, Liu J, Zhang J. Microstructure and property of a functionally graded aluminum silicon alloy fabricated by semi-solid backward extrusion process. Mater Sci Eng A 2015;624:229–38.

https://doi.org/https://doi.org/10.1016/j.msea.2014.11.044.

[50] Natori K, Utsunomiya H, Tanaka T. Improvement in formability of semi-solid cast hypoeutectic Al-Si alloys by equal-channel angular pressing. J Mater Process Technol 2017;240:240–8. https://doi.org/10.1016/J.JMATPROTEC.2016.09.022.

[51] Song D, Wang G, Zhou Z, Klu EE, Gao B, Ma A, et al. Developing a high-strength Al–11Si alloy with improved ductility by combining ECAP and cryorolling. Mater Sci Eng A 2020. https://doi.org/10.1016/j.msea.2019.138880.

[52] Ben DD, Ma YR, Yang HJ, Meng LX, Shao XH, Liu HQ, et al. Heterogeneous microstructure and voids dependence of tensile deformation in a selective laser melted AlSi10Mg alloy. Mater Sci Eng A 2020;798:140109. https://doi.org/10.1016/J.MSEA.2020.140109.

[53] Hadadzadeh A, Shalchi Amirkhiz B, Odeshi A, Li J, Mohammadi M. Role of hierarchical microstructure of additively manufactured AlSi10Mg on dynamic loading behavior. Addit Manuf 2019. https://doi.org/10.1016/j.addma.2019.04.012.

[54] Kong D, Dong C, Wei S, Ni X, Zhang L, Li R, et al. About metastable cellular structure in additively manufactured austenitic stainless steels. Addit Manuf 2021;38:101804. https://doi.org/https://doi.org/10.1016/j.addma.2020.101804.

[55] Li Z, Li Z, Tan Z, Xiong DB, Guo Q. Stress relaxation and the cellular structure-dependence of plastic deformation in additively manufactured AlSi10Mg alloys. Int J Plast 2020;127:102640. https://doi.org/10.1016/J.IJPLAS.2019.12.003.

[56] Fedotova D, Khamidullin R, Shlyannikov V. Inversion of dislocation densities under mixed mode fracture. Eng Fail Anal 2022;138:106311. https://doi.org/https://doi.org/10.1016/j.engfailanal.2022.106311.